

19/10/04

19/10/04

**STUDIES OF FLUORIDE DEPOSITION IN THE  
DENTAL ENAMEL FOLLOWING THE USE OF  
FLUORIDE-CONTAINING GELS BY (p, $\alpha$  $\gamma$ )  
NUCLEAR REACTION**

By

**Annahita Suheil Nasr**

19/10/04

Supervisor

**Dr. Dia-Eddin Arafah, Prof.**

تعتمد كلية الدراسات العليا  
هذه النسخة من الرسالة  
التوقيع: مس التاريخ: 19/10/04

**Submitted in Partial Fulfilment of the Requirements for  
The Master's Degree of Science in Physics**

**Faculty of Graduate Studies  
University of Jordan**

**December 2004**

All Rights Reserved - Library of University of Jordan - Center of Thesis Deposit

This thesis/dissertation (Studies of fluoride deposition in the dental enamel following the use of fluoride-containing gels by (p, $\alpha$ ) nuclear reaction) was successfully defended and approved on 2/12/2004

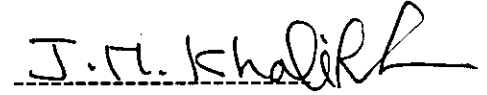
**Committee Members**

Dr. Dia-Eddin Arafah; Chairman  
Prof. of Experimental  
Solid State Physics

**Signature**



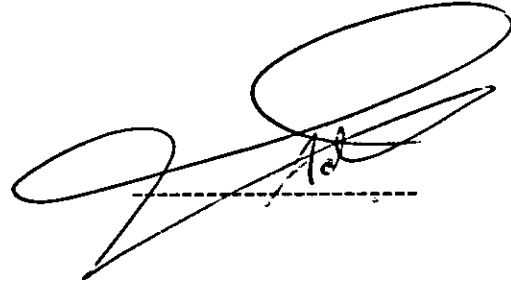
Dr. Jamil Khalifeh; Member  
Prof. of Theoretical  
Solid State Physics



Dr. Issa Shahin; Member  
Prof. of Molecular Spectroscopy



Dr. Adnan Othman; Member  
Associate Prof. of Experimental  
Solid State Physics  
(Yarmouk University)



تعتمد كلية الدراسات العليا  
هذه النسخة من الرسالة  
التوقيع... التاريخ... ٢٠٠٤/١٠/٢٠

*“...and He creates other things beyond your  
knowledge...”*  
*The Holy Qur’an,[16:8]*

## DEDICATION

*This work is dedicated to my parents, for this could never see light without your unlimited encouragement and unconditional love, I will never forget that.*

*This dedication also goes to my sister Maryam and my brother Esam, you were the smile that made things easier.*

## *ACKNOWLEDGEMENT*

---

It is great pleasure to acknowledge my gratitude and express my deep respect and appreciation to my supervisor, prof. Dia' El Din Arafeh, for his continuous encouragement and guidance throughout the period spent in this work. I would like also to extend my profound gratitude to the discussion committee for their endless efforts and limitless time.

Patience and generous help of the staff of JUVAC, Mr. Abdullah Mahmoud, Eng. Salem Kharabshih and Eng. Adel Amro, were also of a precious value to me indeed.

Thanks are always due to my colleagues in Physics department; especially, Rami Zrekat, Luay Barham, Al-Layth Al-Drabee, and Abdullah Mahasneh and Al-Laith Darabee'. It is my pleasure to acknowledge their assistance throughout last year.

Finally, it is my pleasure to acknowledge my indebtedness and my deep feelings toward my family. Their love was necessary for this undertaking to be carried out.

*Annahita S. Nasr*

## *List of Contents*

<b>Subjects</b>	<b>Page</b>
Committee decision	ii
Dedication	iii
Acknowledgement	iv
List of contents	v
List of tables	vi
List of figures	vii
Abstract in English	ix
 <b><i>INTRODUCTION</i></b>	 <b>1</b>
 <b><i>LITERATURE REVIEW</i></b>	 <b>3</b>
 <b><i>THEORETICAL BACKGROUND</i></b>	 <b>11</b>
 <b><i>EXPERIMENTAL</i></b>	 <b>29</b>
 <b><i>RESULTS AND DISCUSSION</i></b>	 <b>40</b>
 <b><i>CONCLUSION AND RECOMMENDATIONS</i></b>	 <b>59</b>
 <b><i>REFERENCES</i></b>	 <b>61</b>
 <b><i>ABSTRACT IN ARABIC</i></b>	 <b>64</b>

<b>LIST OF TABLES</b>
-----------------------

<i>Table Caption</i>	<i>Page</i>
<b>Table (1):</b> Mean values and standard deviation for fluoride concentration ( $\mu\text{g g}^{-1}$ ) in dentine for different teeth types and states.	9
<b>Table (2):</b> Relationship between enamel fluoride content and caries prevalence in young adults.	25
<b>Table (3):</b> Channel number, Kinematic factor and surface scattering energy E1 for calibration sample.	33
<b>Table (4):</b> Brief description of the subject tooth samples.	35
<b>Table (5):</b> Quantitative analysis for determining the basic elements in teeth.	41
<b>Table (6):</b> Values of the thickness traversed in both the standard $\text{CaF}_2$ and tooth samples $\text{Ca}_{10}(\text{PO}_4)_6(\text{OH})_2$ at each incident proton energy.	45

<b>LIST OF FIGURES</b>
------------------------

<i>Figure Captions</i>	<i>Page</i>
<b>Figure (1):</b> Measured F concentration profiles for treated teeth.	4
<b>Figure (2):</b> Torrisi results of F depth profile in the dental enamel.	5
<b>Figure (3):</b> Energy spectrum of protons from the $^{19}\text{F}(\alpha, p)^{22}\text{Ne}$ nuclear reaction at an incident energy of 2325 keV and reaction angle $135^\circ$ . (Borgardt et al, 1998)	6
<b>Figure (4):</b> Measured laboratory differential reaction cross sections for the $p_0$ proton group from the $^{19}\text{F}(\alpha, p)^{22}\text{Ne}$ nuclear reaction at a mean angle of $135^\circ$ .	7
<b>Figure (5):</b> Measured laboratory differential reaction cross sections for the $p_1$ proton group from the $^{19}\text{F}(\alpha, p)^{22}\text{Ne}$ nuclear reaction at a mean angle of $135^\circ$ .	7
<b>Figure (6):</b> Typical $\gamma$ -ray spectrum obtained after the bombardment of a tooth sample with proton energy of 2.4 MeV. (Carvalho et al, 2001).	9
<b>Figure (7):</b> Schematic diagram of the geometry of nuclear reaction.	10
<b>Figure (8):</b> Differential cross section.	13
<b>Figure (9):</b> Hypothetical nuclear reaction as a function of energy for a non-resonant reaction and a resonant reaction ( Mazzoldi & Arnold, 1987)	14
<b>Figure (10):</b> Simplified energy-level diagram for the $^{19}\text{F}$ , $p$ , $^{20}\text{Ne}$ , $^{16}\text{O}$ ( Amsel & Lanford, 1984).	15
<b>Figure (11):</b> Cross section versus incident proton energy at scattering angle of $150^\circ$ for $^{19}\text{F}(p, \alpha)^{16}\text{O}$ reaction.	16
<b>Figure (12):</b> Schematic diagram of the main principles involved in the kinematics of a nuclear reaction.	17
<b>Figure (13):</b> Schematic representation of an elastic collision between a projectile and a stationary target atom.	23



<b>LIST OF FIGURES</b>
------------------------

<i>Figure Captions</i>	<i>Page</i>
<b>Figure (14):</b> Photomicrographs of the deposit of calcium fluoride adsorbed on sound human enamel after 5-min treatment with the fluoridated solution (Navarro et al, 2001).	28
<b>Figure (15):</b> Schematic diagram for the Van de Graff Accelerator used in the experiment (JUVAC).	29
<b>Figure (16):</b> Diagram of collimating slits and beam viewer (Chu et al, 1978).	31
<b>Figure (17):</b> Schematic illustration of the electronic detection setup.	32
<b>Figure (18):</b> RBS spectrum of a calibration sample.	33
<b>Figure (19):</b> The Linear relationship between the energy of scattered particles and channel number	34
<b>Figure (20):</b> Derivative of RBS spectrum of the calibration sample.	35
<b>Figure (21):</b> RBS spectrum of tooth enamel after bombarding the sample with 2 MeV $^4\text{He}$ .	40
<b>Figure (22):</b> Stopping powers of protons in $\text{CaF}_2$ and hydroxyapatite $\text{Ca}_{10}(\text{PO}_4)_6(\text{OH})_2$	43
<b>Figure (23):</b> $\alpha$ -spectrum emanating from $\text{CaF}_2$ .	43
<b>Figure (24):</b> Depth values traversed at each incident proton energy.	46
<b>Figure (25-28):</b> Respective $\alpha$ -spectra obtained after bombarding untreated teeth $T_1$ , $T_2$ , $T_3$ and $T_4$ with a proton beam.	47
<b>Figure (29):</b> Relative fluoride concentrations in untreated tooth samples versus incident proton energy.	51
<b>Figure (30):</b> $\alpha$ -spectra obtained after bombarding a tooth sample $T_1$ (treated with NaF containing dentifrice) with a proton beam.	52
<b>Figure (31):</b> $\alpha$ -spectra obtained from bombarding a tooth sample $T_1$ (treated with SMFP containing dentifrice) with a proton beam.	53
<b>Figure (32-35):</b> Respective relative fluoride concentrations in $T_1$ , $T_2$ , $T_3$ and $T_4$ (before treatment, after treatment with NaF, and after treatment with SMFP).	54

***STUDIES OF FLUORIDE DEPOSITION IN THE DENTAL  
ENAMEL FOLLOWING THE USE OF FLUORIDE-CONTAINING  
GELS BY  $(p, \alpha\gamma)$  NUCLEAR REACTION***

*By*  
***Annahita Suheil Nasr***

*Supervisor*  
***Professor Dia-Eddin Arafah***

***ABSTRACT***

Dentists and physicists have analyzed with nuclear physical methods the fluoride uptake after application of dental enamel caries preventive agents. The purpose of this research is, however, to study the amount of fluoride retained within samples of different human teeth after NaF and SMFP containing dentifrices application. The  $^{19}\text{F} (p, \alpha\gamma) ^{16}\text{O}$  reaction was used as the analytical method in the resonant region, with a proton beam of energy of 1350 keV from the Jordan University Van de Graaff Accelerator, JUVAC, to record the  $\alpha$ -particles emitted at 7071 keV. Fluoride concentration was determined by comparing the  $\alpha$  yield emitted by the dental enamel with that emitted by a standard  $\text{CaF}_2$  specimen. It is shown that fluoride concentrations depend on the age and dietary habits of the patient. However, Fluoride is profiled in the tooth samples to a depth of (1  $\mu\text{m}$ ) and it is indicated that fluoride concentration in a single sample decreases to a certain depth and then increases. Fluoride uptake by samples treated with NaF containing dentifrice depends on the fluoride pre-concentration of these samples; while fluoride uptake by samples treated with SMFP containing dentifrice were remarkably greater.

603373

## CHAPTER ONE

### 1.1 General Introduction

The incidence of dental caries over different range of ages and individuals exhibits large variations, which have been attributed to dietary habits, drinking water and environmental contamination. However, the concentration of trace elements in teeth, as well as their interrelationships, seem to play a key role in the health of human dentition. It is well known that fluoride has a remarkable effect on caries prevention; it decreases the solubility of tooth structure in acidic conditions making teeth more resistant to decay, (Jenkins, 1967). A fluoride concentration study indicated that increased levels of fluoride in the enamel are associated with reduced levels of dental caries, (Curson et al, 1977). It is believed that fluoride is the most reactive chemical element and cannot be freed from its compounds by chemical means. Fluoride is not a rare element and it makes up, an estimated 0.065% of the Earth's crust. The element Fluorine,  $^{19}F$  is the only stable isotope that exists in tooth enamel as fluorhydroxyapatite ( $Ca_{10}(PO_4)_6(OH)_2-F$ ). Therefore, applications of ion beam analysis are restricted, since no other stable isotope with different nuclear properties can be separated and used as a tracer inside the tooth enamel. (Coote, 1992).

The objective of this investigation is to explore the possibility of developing a reliable non-destructive method for determining the concentration of fluoride as a function of the depth in the enamel, the outer layers of human teeth; which had been subjected to various fluoride treatments. The methods that have been previously used include acid etching, grinding, and electron probing. Such methods do not have adequate depth resolution and are difficult and time consuming to perform. In addition, the acids etching and surface grinding methods destroy the portion of the sample analyzed; whence are destructive methods (Mandler et al, 1973).

Other studies showed that the Rutherford Backscattering is ineffective in obtaining the concentration versus depth profile of fluoride in the presence of heavier elements composing the tooth enamel such as Calcium and Oxygen (Kuperus, 1965). However, nuclear resonance reaction was selected to perform these measurements without removal of the outer layers of the subject teeth. One of the most common nuclear reactions that have been employed for fluoride analysis and its depth distribution in the enamel surface in this work is the resonant nuclear reaction  $^{19}\text{F}(p, \alpha)^{16}\text{O}$  with varied incident proton energy between 1350 keV and 1400 keV, using the broad resonance at 1350 keV. The concentration profiles of the other trace elements in teeth, such as Sodium and Magnesium, have been measured by employing the Proton Induced X-ray Emission (PIXE), (Chaudhri and Crawford, 1981).

## **1.2 Literature Review**

### ***1.2.1 Introduction***

Studies which provide fundamental data for ion beam analysis and depth profiling in the outer few micrometer of materials showed that the nuclear reactions are the most suitable (Coote, 1992). However, the first application of ion beam analysis of fluoride goes to Sippel and Glover in 1960. They needed new techniques for determining light elements in silicate rocks and the measurements of 6-7 MeV gamma-rays from proton bombardment was their chosen method for fluoride detection and measurement.

### ***1.2.2 Previous Work***

#### **1) Mandler et al, 1973**

The gamma-ray induced from proton bombardment of fluorine was discovered in the 1950s. The high energy  $\alpha$ -radiation from the  $^{19}\text{F}(p,\alpha\gamma)^{16}\text{O}$  reaction interferes with gamma-ray spectrometry, since they are produced prolifically from minute amounts of fluoride in targets.

Tooth enamel was an obvious target and the first application of depth profiling to tooth enamel was published in 1973 by (Mandler et al). The  $^{19}\text{F}(p,\alpha\gamma)^{16}\text{O}$  reaction has been used to measure the concentration profile of fluoride in tooth enamel. By determining the intensity of the 6.13 MeV gamma-ray produced with a high resolution Ge(Li) detector by the 672 keV resonance and comparing these intensities with those obtained using standards like Teflon and  $\text{CaF}_2$ , the fluoride concentration was measured to a depth of 2.1  $\mu\text{m}$  in three teeth: One treated with an aqueous solution of 2.5%  $\text{K}_2\text{ZrF}_6$ , one with 2.6%  $\text{NaF}$ , and one with 1.23% acidulated fluorophosphates. The differential depth resolution was better than 0.1  $\mu\text{m}$  at the surface of the teeth. The results of the measurements are shown in figure (1)

fluorophosphates. The differential depth resolution was better than  $0.1 \mu\text{m}$  at the surface of the teeth. The results of the measurements are shown in figure (1)

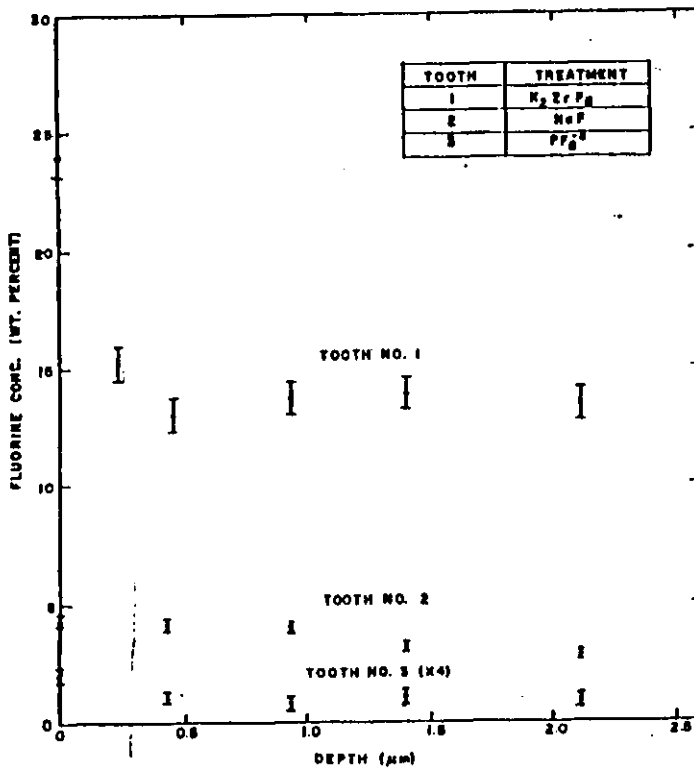


Figure (1): measured fluoride concentration profiles for the three treated teeth

In both the tooth treated with  $K_2ZrF_6$  and that treated with acidulated fluorophosphates, the fluoride concentration drops rapidly with depth to about 50% of the surface concentration. This happens at a depth of about  $0.4 \mu\text{m}$  cf. figure (1). However, in the NaF treated tooth the fluoride concentration exhibits a much slower decrease with depth. In addition to the variation in the shapes of the fluoride profiles, the magnitude of the concentrations produced by the three fluoride solutions vary over a factor of about 50. The  $K_2ZrF_6$  solution, however, produced the highest fluoride concentration.

## 2) Torrisi et al, 1986

The  $^{19}\text{F}(\text{P},\alpha)^{16}\text{O}$  reaction yields high energy  $\alpha$ -particles (6969) keV at incident proton energy (1350) keV which is well separated from other reactions of similar products. Torrisi et al (1986) used this nuclear reaction to study the depth profiling of fluoride in hemi-arc tooth enamel belonging to a 62-year old patient. The  $\alpha$ -particles were detected by a surface barrier detector. The yield of the  $\alpha$ -particles was compared with a standard sample that was prepared by squeezing powder chromium fluoride  $\text{CrF}_3$  into a stainless steel cylinder. Samples in the experiment were tilted by an angle of  $(45^\circ)$ , while the detector was placed at an angle of  $(150^\circ)$ , both with respect to the incident beam direction, where the produced yield was maximum at this proton energy. The proton beam current was reduced to (50) nA to eliminate the radiation damage effect on the target. The distribution of fluoride in the dental enamel is given in figure (2)

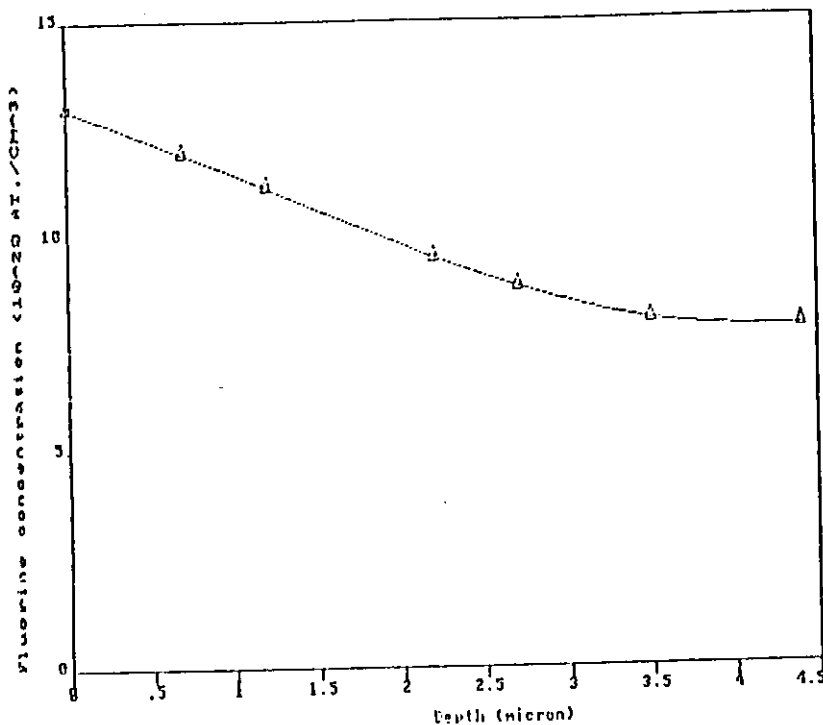


Figure (2): Results of fluoride depth profile in the dental enamel Torrisi et al, 1986.

The depth profile presents strong fluoride accumulation in the first micron followed by progressive decrease. The results show a correlation between F concentration in the enamel and the different environment exposure.

### 3 )Borgardt et al, 1998

Nuclear reactions provide a useful technique for detecting and depth profiling of light elements in samples where conventional Rutherford Backscattering is ineffective due to the presence of heavy elements. Among the light elements,  $^{19}\text{F}$  is amongst that encountered. In their work Borgardt et al (1998) have presented cross section measurements which can be used to determine and depth profile  $^{19}\text{F}$  in thin films using the  $^{19}\text{F}(\alpha, p_0)^{22}\text{Ne}$  at a resonance energy of 2313 keV.

A thin  $\text{YF}_3$  film on a carbon backing was bombarded with a beam of  $^4\text{He}$  ions, and the protons from the reaction were collected using a silicon surface barrier detector, placed at  $135^\circ$  relative to the incident beam direction. Figure (3) shows the energy spectrum of protons from the  $^{19}\text{F}(\alpha, p)^{22}\text{Ne}$  reaction.

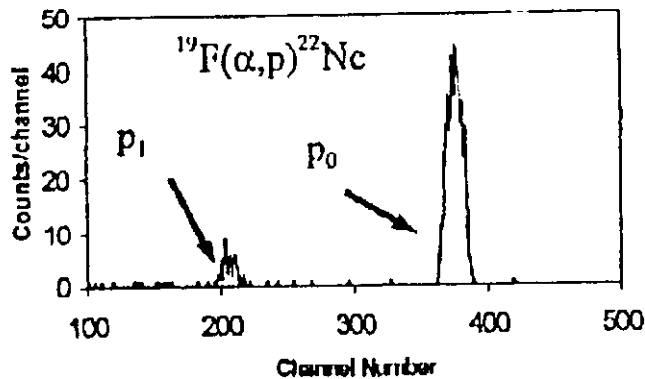


Figure (3): energy spectrum of protons from the  $^{19}\text{F}(\alpha, p)^{22}\text{Ne}$  nuclear reaction at an incident energy of 2313 keV and reaction angle  $135^\circ$ , after Borgardt et al, (1998).



## CHAPTER TWO

### *Theoretical background*

#### 2.1 Theory of nuclear reaction

##### *2.1.1 Introduction*

Among the different interactions taking place when a charged particle beam impinges onto a target, is the nuclear reaction, which represents an important role in tracing small amounts of impurities with low atomic mass in a substrate with a higher atomic mass that is usually difficult to detect by Rutherford Backscattering RBS technique due to system and mass resolutions.

The geometry of the nuclear reaction analysis is shown in a schematic diagram in figure (7). An incident high mono-energetic particle, or projectile, of mass  $M_1$ , energy  $E_0$ , and atomic number  $Z_1$  bombards a target nucleus of mass  $M_2$ , and atomic number  $Z_2$  through the nuclear reaction  $M_2(M_1, M_3)M_4$  where  $M_4$  is the mass of the residual nucleus and  $M_3$  is the mass of the outgoing particle that leaves the target under the scattering angle  $\theta$ , namely:

$$(1) \quad (M_1 + M_2)C^2 \longrightarrow (M_3 + M_4)C^2 + Q$$

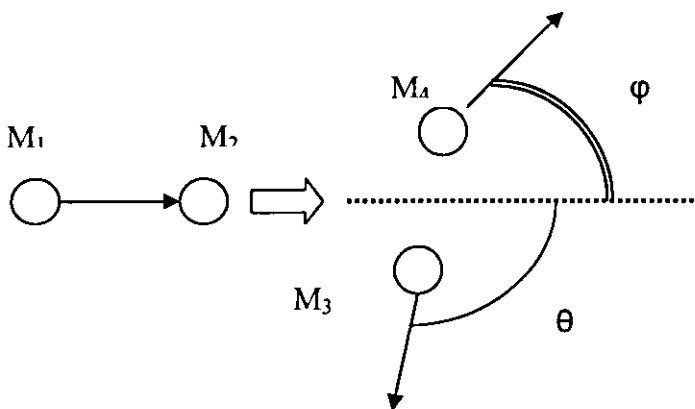


*Figure (7): Schematic diagram of the geometry of nuclear reaction*

Experimentally, resonant reactions are of particular interest in surface analysis because depth information can be obtained. This is achieved if the beam is first set to the energy of resonance to probe the surface. Then by increasing the beam energy slightly over resonance, the reaction will tend to occur below the surface due to energy loss of the beam while traversing the target. The resonance energy, being characteristic of a particular reaction, can also be used in some cases to identify elements within the target. Moreover, the narrow width of a nuclear reaction resonance provides a greatly improved way of measuring changes in the beam energy as it penetrates the target and equivalently provides improved depth resolution for depth distribution measurements.

### 2.1.5 Concentration profile determination

In practical situations, depth profiling can be obtained when nuclear resonant reactions are employed. Figure (12) shows the parameters involved in analyzing a thick target when a beam of incident energy  $E_0$  falls onto a low-mass target (Arafah and Meyer, 1988):

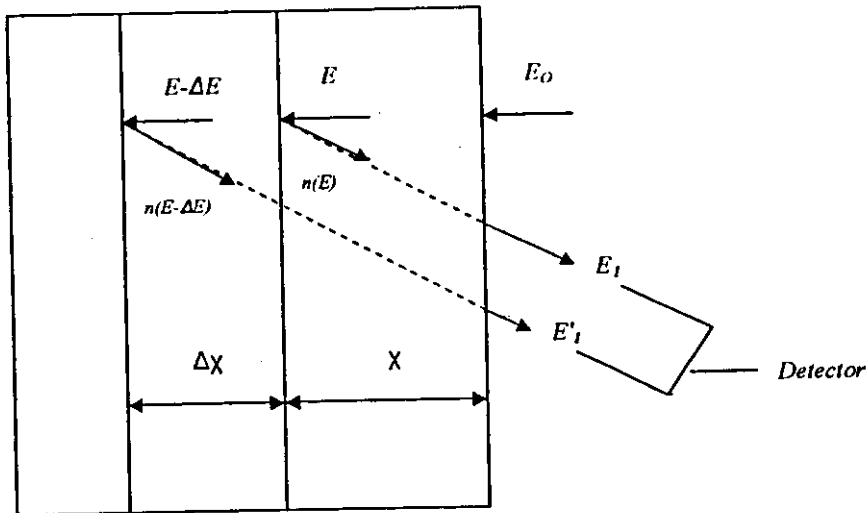


Figure (12): schematic diagram showing the main principles involved in the kinematics of a nuclear reaction

The energy of the detected particles resulting from the surface of the target is described by equation (5):

$$E'_o = n(E_o) = \left[ K_1 + \sqrt{K_1^2 + K_2} \right]^2$$

See equations in (6).

However, the detected energies for particles reaching the detector from reactions taking place at depths  $\chi$  and  $\chi + \Delta\chi$  are, respectively,  $E_l$  and  $E'_l$  cf. figure (12).

In general, particles of energy  $E$  will suffer an energy loss  $\Delta E$  when traversing a slab in the target of thickness  $\Delta\chi$  due to several contributions arising from the incident particle's interaction with the target's electrons, i.e. electronic energy loss, the atoms of the target as a whole, i.e. the nuclear energy loss, or even by exchanging the incident particle's electrons with the target. However, the total energy loss is the sum of these individual contributions.

The stopping cross section of the target material  $\varepsilon$  is given by:

$$\varepsilon = \frac{1}{N} \frac{dE}{dx} \quad (8)$$

where  $\frac{dE}{dx}$  is the mean energy loss per unit length below the surface in the target (or the stopping power), and  $N$  is the atomic density of the target. If however the material of the target is a compound of elements,  $m$ , weighed to their concentration  $C_i$  then according to Bragg's additive rule, the total stopping cross section in the target is:

$$\varepsilon_t = \sum_m C_i \varepsilon_i \quad (9)$$

The distance  $x$  traversed along the inward (in) path of the normally incident particles shown in figure (12) before the reaction takes place at energy  $E$ , and along the outward (out) path with a detection angle  $\theta$  after the reaction takes place is given by:

$$x = \frac{1}{N} \int_E^{E_2} \frac{1}{\epsilon_{in}} dE = \frac{|\cos \theta|}{N} \int_{E_1}^{n(E)} \frac{1}{\epsilon_{out}} dE \quad (10)$$

Where  $\epsilon_{in}$  and  $\epsilon_{out}$  are the stopping cross sections along the inward and outward paths, respectively.

Similarly, at depth  $x + \Delta x$  resulting from the incident energy  $E - \Delta E$ , equation (10) becomes:

$$x + \Delta x = \frac{1}{N} \int_{E - \Delta E}^{E_2} \frac{1}{\epsilon_{in}} dE = \frac{|\cos \theta|}{N} \int_{E_1'}^{n(E - \Delta E)} \frac{1}{\epsilon_{out}} dE \dots \dots \dots (11)$$

Since the energy  $E$ , inside the sample is not an experimentally accessible quantity, whereas the detected energy  $E_1$  is accessible, therefore, equation (10) has to be solved for  $E_1$ , that is if  $\epsilon_{in}$  and  $\epsilon_{out}$  are both known. Moreover, the slab  $\Delta x$  width is not known, but on the other hand, particles coming from this slab and falling into one channel of the multi-channel analyzer (MCA) have energy  $|E_1 - E_1'| = W$ , where  $W$  is the channel width. This means that equation (11) contains only one unknown parameter,  $\Delta E$ , provided that  $E$  is known from equation (10). Equation (11) can then be expanded and reduced using equation (10), so that, finally,

$$\Delta x = \frac{1}{N} \int_{E - \Delta E}^E \frac{dE}{\epsilon_{in}} = \frac{|\cos \theta|}{N} \left( \int_{E_1'}^E \frac{dE}{\epsilon_{out}} + \int_{n(E - \Delta E)}^{n(E)} \frac{dE}{\epsilon_{out}} \right) \quad (12)$$

Equation (12) states that the incoming particles lose their energy from  $E$  to  $E - \Delta E$  in the slab of thickness  $\Delta x$ , this energy is governed by the integral of the inverse stopping cross section which is practically a smooth function of energy (Anderson and Ziegler, 1977). On the other hand, particles reaching the detector after traversing the slab along the outgoing path should fall into one channel of width  $W$  at the MCA which is of the order of several keV.

Assuming that  $\Delta E$  and  $\Delta x$  are small compared to  $\varepsilon(E)$ , then the integrand in the first term of the right hand of equation (12) is cancelled and can be approximated to:

$$\Delta x = \frac{1}{N} \frac{1}{\varepsilon_{in}(E)} \Delta E \quad (13)$$

The second term on the right hand side of equation (12) can be approximated as follows:

Given that  $(E_1 - E'_1) = \pm W$ , then:

$$\int_{E'_1}^{E_1} \frac{1}{\varepsilon_{out}} dE = \pm \frac{1}{\varepsilon_{out}(E_1)} W \quad (14)$$

And if it is further assumed that  $n(E)$  has a weak dependence on the energy, then:

$$\int_{n(E)}^{n(E-\Delta E)} \frac{1}{\varepsilon_{out}} dE = \frac{\Delta E}{\varepsilon_{out}(n(E))} * \left. \frac{dn(E)}{dE} \right|_E \quad (15)$$

Substituting equations (13), (14) and (15) in (12) allows one to obtain the following form:

$$\Delta x = \frac{1}{N} \frac{1}{\varepsilon_{in}(E)} \Delta E = \frac{|\cos \theta|}{N} \left\{ \pm \frac{1}{\varepsilon_{out}(E_1)} W - \frac{\Delta E}{\varepsilon_{out}(n(E))} * \left. \frac{dn(E)}{dE} \right|_E \right\} \quad (16)$$

In this case equation (16) can be rearranged and rewritten as: (D. -E. Arafah and Meyer, 1988)

$$\Delta E = \Delta x N \varepsilon_{in}(E) = \frac{\pm |\cos \theta| W}{\varepsilon_{out}(E_1)} \left/ \left( \frac{1}{\varepsilon_{in}(E)} + \frac{|\cos \theta|}{\varepsilon_{out}[n(E)]} \frac{dn(E)}{dE} \right) \right|_E \quad (17)$$

One of the general properties of nuclear reactions is its non-destructive quantitative analysis of the first microns of the target which results in reaction yield (or number of counts) that is dependent on the reaction cross section and is a function of the incident energy but not on the physical or the chemical states of the atom.

In general, the reaction yield resulting from a nuclear reaction of element A in a target of thickness  $\Delta x$  taking place at a specific channel with an energy  $E_1$  using a multi-channel analyzer is given by:

$$H_A(E_1) = \Omega Q \sigma_A(E, \theta) C_A N \Delta x \quad (18)$$

Where  $\Omega$  is the detector's solid angle;  $Q$  is the total number of the incident particles and  $C_A$  is the concentration of element A;  $N$  is the volume density of the target, and  $\sigma$  is the reaction differential cross section. Using equation (17), equation (18) becomes:

$$H_A(E_1) = \Omega Q \sigma_A(E, \theta) \frac{C_A W |\cos \theta|}{\varepsilon_{in}(E) \varepsilon_{out}(E_1)} \left/ \left( \frac{1}{\varepsilon_{in}(E)} + \frac{|\cos \theta|}{\varepsilon_{out}[n(E)]} \frac{dn(E)}{dE} \right) \right|_E \quad (19)$$

Equation (19) indicates that the concentration  $C_A$  as a function of depth can be calculated from the measured yield if the reaction cross section as a function of energy is known.

However, in quantitative analysis for the determination of the concentration of a certain element, usually a reference material (standard) of known concentration is measured and then the concentration of the actual sample (target) is deduced. (Savidou, et al, 1999).

The energy of the detected  $\alpha$ -particles is calculated by subtracting the energy loss  $\Delta E_\alpha$  in a slab of thickness  $\Delta x$  from that of the  $\alpha$ -particles coming out of the nuclear reaction, best described in the following equation:

$$\Delta E_\alpha = \varepsilon_\alpha \frac{\Delta x}{\cos \theta} \quad (20)$$

Where  $\varepsilon_\alpha$  is the stopping power of  $\alpha$ -particles in the material layer.

Since  $\alpha$ -particles will have the same energy at depths  $x_s$  and  $x_t$  (subscript  $s$  denotes standard sample, and subscript  $t$  denotes target sample). Therefore, the fraction of energy lost in a layer of thickness  $\Delta x$  in the standard sample is equal to that in the target sample, namely:

$$\Delta E_{\alpha t} = \Delta E_{\alpha s} \quad (21)$$

Using equations (18) and (20) and substituting in equation (21), one obtains:

$$C_t(x_t) = C_s \frac{H_t \varepsilon_{\alpha t}}{H_s \varepsilon_{\alpha s}} \quad (22)$$

Where  $C_t(x_t)$  is the concentration of an element in the target sample as a function of depth,  $C_s$  is the concentration of the same element in the standard sample.  $H_t$  and  $H_s$  are yields of  $\alpha$ -spectra in target and standard samples, respectively. Similarly,  $\varepsilon_{\alpha t}$  and  $\varepsilon_{\alpha s}$  are the stopping powers of  $\alpha$ -particles in target and standard samples, respectively.

## **2.2 Rutherford Backscattering Spectroscopy (RBS)**

Backscattering analysis represents a powerful technique for detecting surface impurities on a light-element substrate. Rutherford backscattering is performed by bombarding a sample target with a monoenergetic beam of high-energy particles, typically helium, with energy of a few MeV. A fraction of the incident atoms scatter backwards from heavier atoms in the near surface region of the target material, and are usually detected with a solid state detector that measures their energies.

The energy of the back-scattered particles is related to the depth and mass of the target atom while the number of backscattered particles detected from any given element is proportional to concentration. This relationship is generally used to generate a quantitative depth profile of the upper 1 to 2  $\mu\text{m}$  of the surface of the sample (Baumann, 2000).

In principle, the kinematics related to RBS are similar to those involved in the nuclear reaction analysis (NRA). Yet, there are some slight modifications to the kinematics of RBS arising from the fact that the backscattered particle, which is identical to the incident particle (or projectile), possesses an energy  $E_1$  equals to  $KE_o$  after an elastic scattering takes place, where  $K$  is the kinematic factor defined as the ratio between the energy of the scattered particle to that of the projectile, given that  $M_2 \geq M_1$  cf. figure (13), (Chu *et al.*, 1978) i.e.:

$$K = \frac{E_1}{E_o} = \left[ \frac{M_1 \cos \theta + (M_2^2 - M_1^2 \sin^2 \theta)^{\frac{1}{2}}}{M_1 + M_2} \right]^2 \quad (23)$$

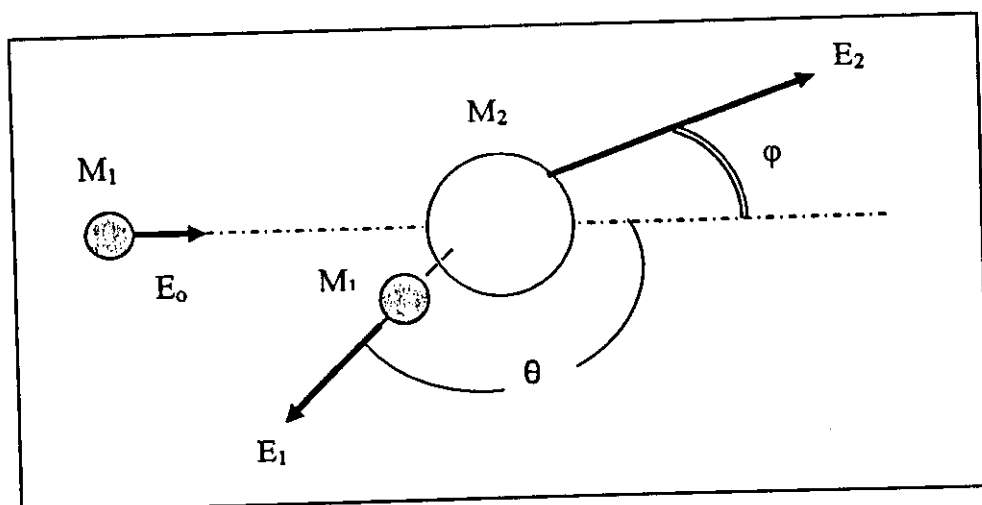


Figure (13): Schematic representation of an elastic collision between a projectile (of mass  $M_1$ , energy  $E_o$ ) and a stationary target atom (of mass  $M_2$ ).



**The Scattering cross section ( $\sigma$ ):**

When a narrow beam impinges on a thin uniform target that is wider than the beam, not all, but only a very few of those incident particles are scattered from the surface of the target, and not all but only a fraction of the scattered particles are detected by an ideal detector that in turn counts each particle scattered in a differential solid angle,  $d\Omega$ , at an angle  $\theta$  from the direction of incidence, therefore the differential scattering cross section,  $d\sigma$ , is defined as:

$$\frac{d\sigma}{d\Omega} = \frac{1}{Nx} \left[ \frac{dQ/d\Omega}{Q} \right], \quad (24)$$

Where:

Q: the total number of incident particles;

dQ: the number of particles recorded by the detector;

N: the volume density of the film of thickness,  $x$ .

Thus  $Nx$  is the surface density of the target.

Assuming that the interaction between the incident and target atoms is elastic, and that the principles of conservation of energy and momentum must be complemented for the Coulomb force that acts during the collision, then the differential cross section under these assumptions can be calculated using Rutherford formula (Chu *et al.*, 1978), namely

$$\frac{d\sigma}{d\Omega} = \left( \frac{Z_1 Z_2 e^2}{4E} \right)^2 \frac{4}{\sin^4 \theta} \frac{\left\{ \left[ 1 - \left( \frac{M_1}{M_2} \right) \sin^2 \theta \right]^{1/2} + \cos \theta \right\}^2}{\left[ 1 - \left( \frac{M_1}{M_2} \right) \sin^2 \theta \right]^{1/2}} \quad (25)$$

Here  $Z_1$  is the atomic number of the projectile with mass  $M_1$ ,  $Z_2$  is the atomic number of the target atom with mass  $M_2$ ,  $e$  is the electronic charge and  $E$  is the energy of the

projectile immediately before scattering. This formula is valid for values in the laboratory frame of reference

### 2.3 Human Teeth

Human teeth consist of three hard substances, arranged in the following order: the outer surface or the enamel, the dentine, and the cementum that covers the root of the tooth. Tooth enamel is the most mineralized tissue of human body; its composition is 96 wt.% inorganic material and 4 wt.% organic material and water. This inorganic material is mainly composed of calcium phosphate related to the hexagonal hydroxyapatite, whose chemical formula is  $\text{Ca}_{10}(\text{PO}_4)_6(\text{OH})_2$  (Le Geros, 1991).

Enamel demineralization is caused by the bacteria which forms the plaque. The bacteria forms a complex community consisting of many types of bacteria, some of which have been isolated and identified. The metabolic activity of this bacteria is responsible for demineralization of the enamel, which can lead to tooth decay; as bacteria ferment sugars. The pH falls, creating an acidic environment, where the enamel becomes more soluble and calcium leaches out of the enamel causing demineralization.

However, tooth enamel can remineralize and decrease its solubility when pH rises in the presence of fluoride, as the ingested fluoride is deposited in the enamel, fluorhydroxyapatite (often also called "firmly-bound fluoride") is formed (Rosin-Gregt et al, 2001). Research has shown that this fluorhydroxyapatite is less susceptible to acid attack than the unmodified hydroxyapatite and it is more resistant to tooth decay.

Studies of the use of topical fluoride applications for the control of dental caries began in the early 1940s. Since that time, it has been generally accepted that there is an inverse relationship between fluoride content of the enamel and the prevalence of dental caries. Table (2) shows an example of this relationship in young naval recruits 17 to 22 years of age (Keene & Perry 2002).

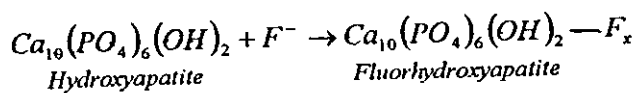
**Table (2): relationship between surface enamel fluoride content and caries prevalence in young adults.**

Number of subjects	Caries Prevalence	Enamel Fluoride Content (ppm)
47	0	3459
31	5-11	2229
29	12-26	1944

At present, fluoride is the only dentifrice additive with significant caries-preventive value. Therefore, it is added to dentifrices in different fluoride compounds such as Sodium Fluoride (NaF), Stannous Fluoride (SnF<sub>2</sub>), and Sodium Mono-fluorophosphate or (SMFP) with an empirical formula (Na<sub>2</sub>PO<sub>3</sub>F). In this work, only (NaF) and (SMFP) are applied to tooth samples since they are the most commercially common active ingredients added to dentifrices used by most people.

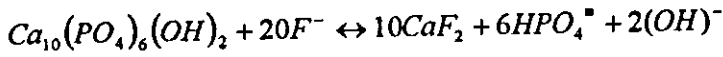
The predominant mechanism of action of fluoride involves its ability to facilitate the remineralization of the demineralized areas of the tooth enamel. Topically applied fluoride diffuses into these demineralized areas and reacts with calcium and phosphate in the unmodified hydroxyapatite composing the tooth to form fluorhydroxyapatite in the remineralization process.

This reaction is best described in the following chemical equation:



However, the nature of the reaction between soluble fluoride and enamel is influenced by a number of factors, including fluoride concentration, the pH of the

solution, and length of exposure. For example, the use of acidic fluoride in sodium fluoride solution greatly favored the formation of calcium fluoride, as indicated in the following chemical equation:



It is noted from the preceding equation that the reaction involves the breakdown of the apatite crystal into its components followed by the reaction of fluoride and calcium ions to form calcium fluoride ( $\text{CaF}_2$ ) with the net loss of phosphate ions from treated enamel. Newer fluoride systems incorporate means to prevent such phosphate loss by using neutral sodium fluoride solutions with fluoride concentrations of 100 ppm or even less to result in the formation of fluorapatite (Christen, 1991).

In a previous study, (Navarro et al, 2001), the calcium fluoride uptake by human enamel after topical application using fluoridated mouth rinses was evaluated using scanning electron microscope (SEM). Photomicrographs showed that none of the samples of the control group had any fluoride deposits on the surface; cf. figure (14A), while in samples treated with fluoridated solutions, amounts of fluoride deposits was obvious as seen in figure (14B).

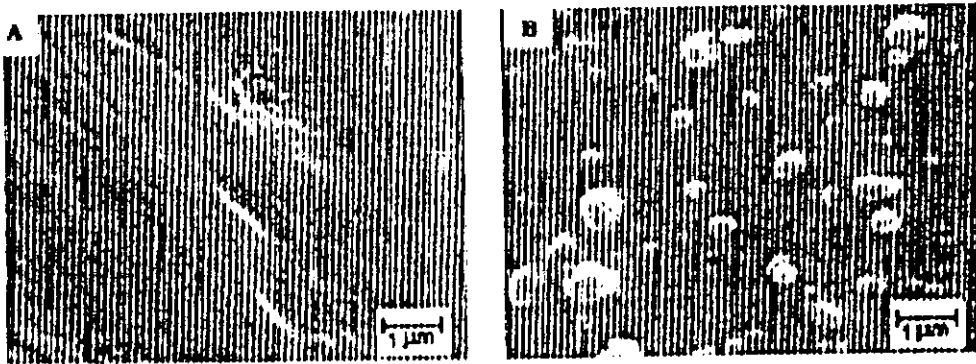


*Figure (14): photomicrographs of the deposit of calcium fluoride adsorbed on sound human enamel after 5-min treatment with the fluoridated solution.  
A: control, B: fluoridated after Navarro et al, (2001)*

## CHAPTER THREE

### *EXPERIMENTAL*

#### 3.1 Experimental Setup

The experiment and measurements were performed at Jordan University Van de Graaff Accelerator (JUVAC). A monoenergetic proton beam bombarded targets of human teeth containing fluoride initiating  $^{19}\text{F}(p,\alpha)^{16}\text{O}$  nuclear reaction. However, the main experimental parts including the Van De Graaff accelerator, the beam line, and the detection system are discussed below.

##### *3.1.1 The Van De Graaff Accelerator*

To obtain high a accelerated ion beam of maximum energy of (4.75 MeV) a Van de Graaff accelerator is used. Schematic diagram of JUVAC is illustrated in figure (15)

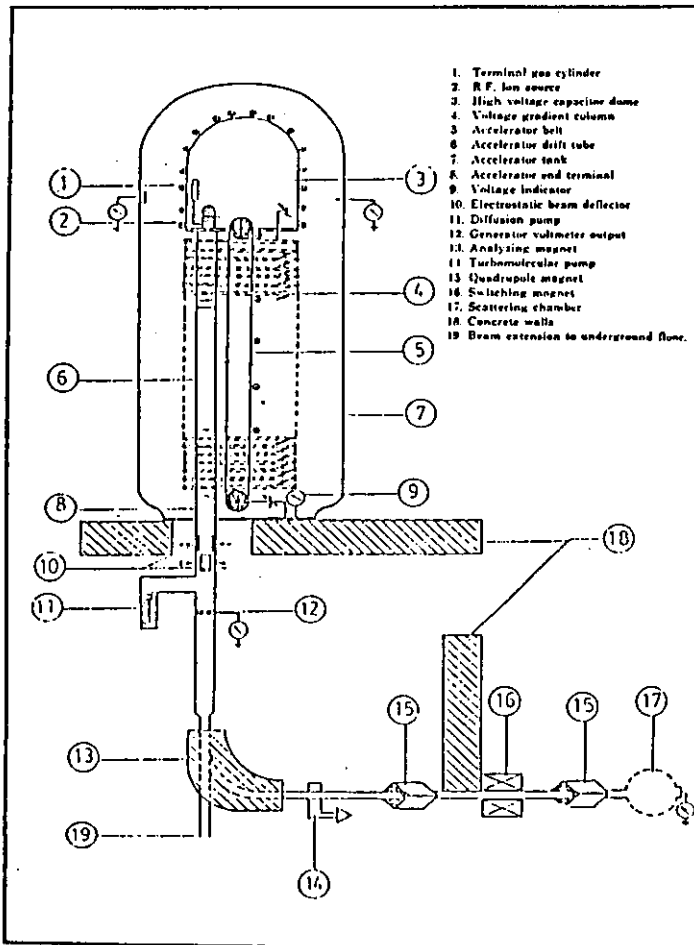


Figure (15): schematic diagram for the Van de Graff Accelerator used in the experiment.

The figure shows the main parts of the accelerator that consist of a high voltage terminal or the capacitor dome (corona cap) (3) which acquires a high electric potential through a concentration of charges transferred to it by an insulating moving belt (5) that increases the potential on the terminal dome as it moves faster. The terminal voltage is  $Q/C$ , where  $Q$  is the charge of the terminal dome and  $C$  is the effective capacitance of the dome.

The dome is connected to ground by a series of resistors referred to as the voltage gradient column (4). It provides a potential gradient and in turn provides a uniform electric field which accelerates the particles through a high vacuum accelerator drift tube (6).

The potential of the terminal dome at JUVAC is controlled by adjusting the magnitude of the discharge current passing between a series of metal rings (corona rings) equally spaced along the high vacuum accelerating tube. A series of coaxial cylindrical electrodes are mounted inside the accelerating tube in order to focus the beam, each electrode is connected to an external corona ring electrode. The ion source is mounted inside the top of the accelerating tube, and can be switched to four different gas bottles. (G. Amstel, et al (1971))

After being accelerated to the desired energy, the charged particles reach the analysing magnet (13) where they will be filtered to the proper energy and deflected through  $90^\circ$  to enter the beam line.

### 3.1.2 The beam line

It is that part of the apparatus, through which the accelerated ions pass after being deflected ( $45^\circ$ ) by the switching magnet (16) to interact with the target.

High vacuum is always desired. This however, requires two vacuum pumps. The first station vacuum pump (11) is located on the beam line, while the second one is located on the target chamber (17) to bring the vacuum inside the target chamber to an appropriate value of the order of ( $10^{-5}$ ) mbar.

The beam of charged particles is steered inside the beam line, using two sets of quadrupole magnets (or magnetic lenses) (15)

It is desired to have sharp edges for the beam of charged particles. Therefore, at least one set of movable, micrometer driven collimating slits is recommended to be used. A typical set of collimation slits is shown schematically in fig. (16)

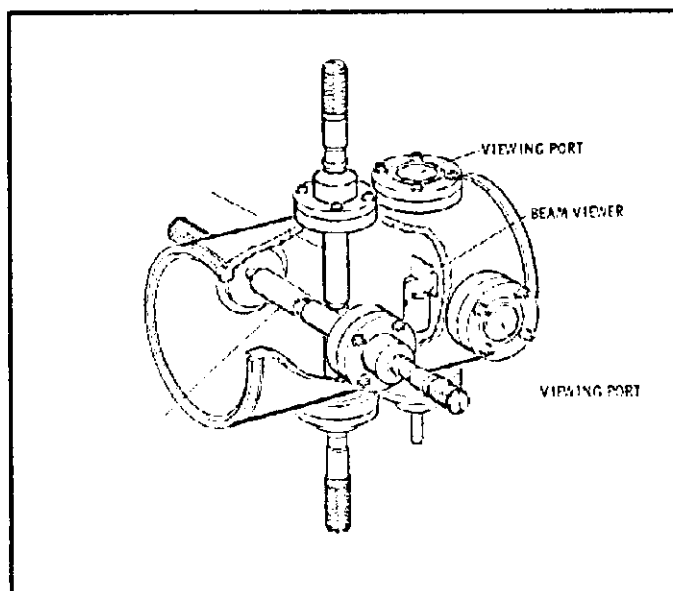


Figure (16): Diagram of collimating slits and beam viewer, after Chu et al, (1978)

At the end of the beam line an aperture is positioned. A beam of protons is normally incident on different samples of human teeth mounted in front of the aperture on a copper made target holder placed in the target chamber.

### 3.1.3 Electronic detection setup

The alpha particles detection system is schematically shown in figure (17), it consists of an Ortec silicon surface barrier detector of 150 mm<sup>2</sup> active area and a minimum sensitive depth of 100  $\mu$ m positioned at an angle of 135° relative to the incident beam direction. The detector was supplied with the necessary voltage of (60) volts by a bias supply.

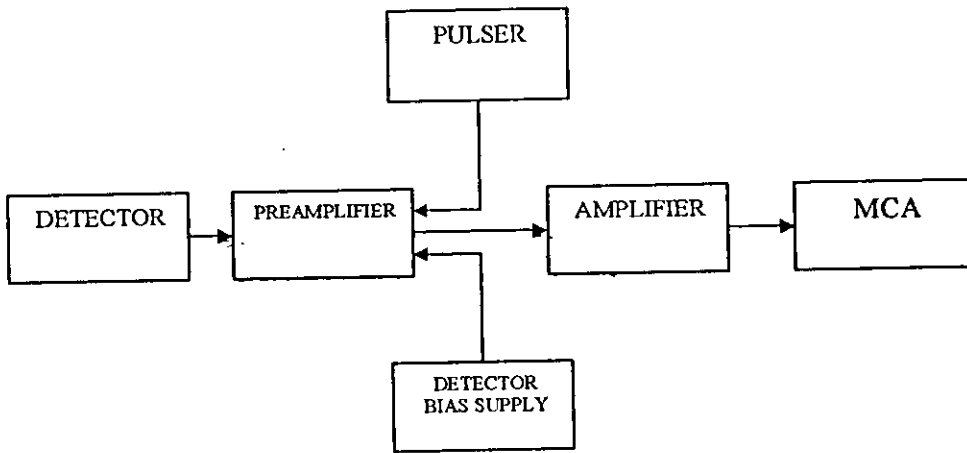


Figure (17): Schematic illustration of the electronic detection setup.

The system also consists of an Ortec charge sensitive preamplifier that produces a voltage pulse with peak amplitude that is proportional to the total charge of the current pulse. An amplifier is then used to expand the range of the peak amplitude, shape the signal of the preamplifier, and maximise the signal-to-noise ratio (SNR). After that, the signal is processed through a multichannel analyzer (MCA) which is



characterized by its ability to work in a pulse-height-analysis (PHA) mode that accumulates the sequence of input pulses by measuring the amplitude of each input event and converting it to a channel number using the analogue-to-digital converter (ADC).

### 3.2 Calibration of the (MCA)

(MCA) provides means for the stored data to be displayed, printed or recalled later for further analysis using convenient computer software (mcd4lap). This is, however, achieved if the (MCA) is calibrated using a sample which consists of several thin films deposited onto a silicon substrate. The sample configuration used here consists of: Si (substrate), Mn film /500nm, Ag film /500nm and an Au film being the uppermost top layer/ 500nm. The sample was bombarded with a beam of accelerated  $\alpha$ -particles of incident energy  $E_0$  equals to 2 MeV, the spectrum accumulated from the scattered  $\alpha$ -particles is shown in fig. (18)

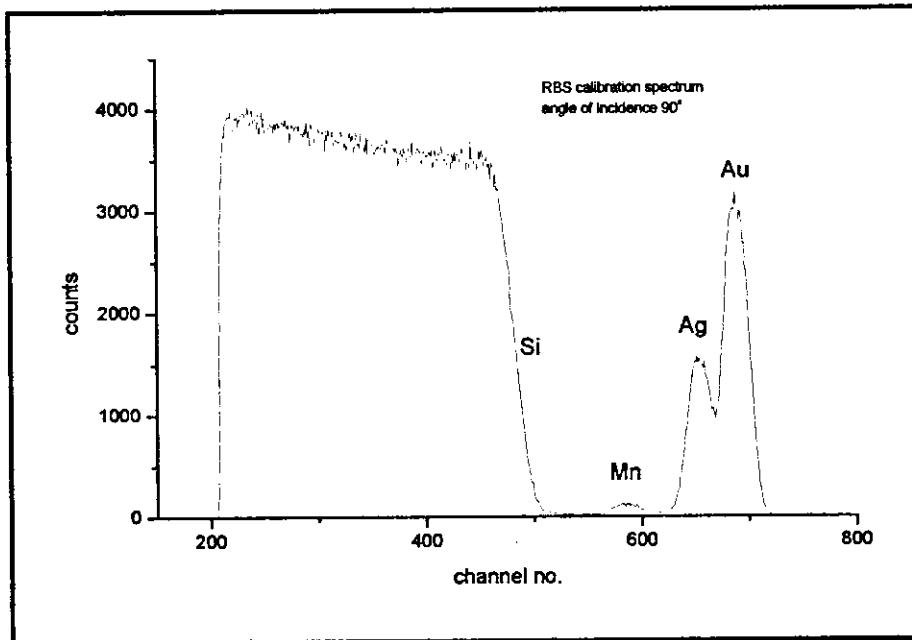


*Figure (18): RBS spectrum of the calibration of sample.*

The channel number corresponding to the surface position of the Si substrate was taken at the half height edge of the Si signal, while that for Mn, Ag and Au films the surface position is represented by the peak position of each respective signal; Table (3). By plotting the data listed in table (3), one obtains a linear relation between the output energy and the corresponding surface position channel number. Fig. (19).

Best described by the equation:

$$E \text{ (keV)} = 3N - 219.2 \quad \text{N: Channel number} \quad (26)$$

**Table (3): Channel number, Kinematic factor and surface scattering energy  $E_i$  for calibration sample.**

<i>Element</i>	<i>Channel no.</i>	<i>Kinematic factor (K)</i>	<i><math>E = KE_o</math> (keV)</i>
Silicon	484	0.61247	1224.94
Gold	699	0.93278	1865.56
Silver	655	0.88062	1761.24
Manganese	586	0.77954	1559.08

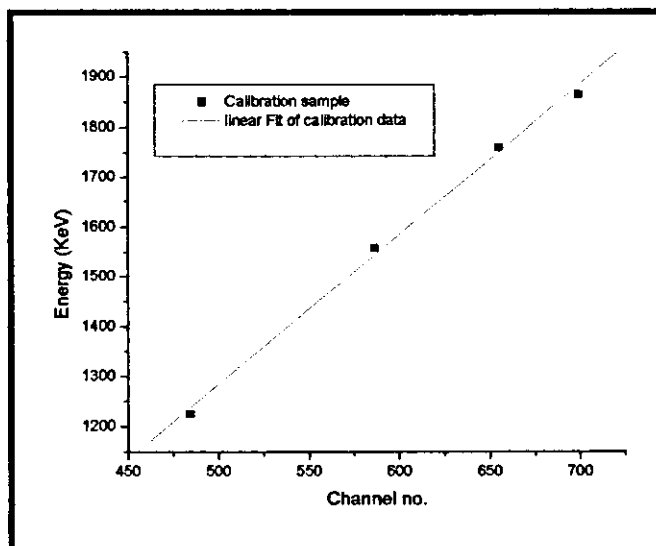


*Figure (19): The linear relationship between the energy of the scattered particles and the channel number*

### 3.3 Detector's Resolution

The surface barrier detector is characterized by its ability to respond to monoenergetic beam; it accumulates an output distribution referred to as the energy response function of the detector. If the width of the distribution is narrow then the detector has a good resolution. This resolution can be measured from the RBS spectrum of the calibration sample after being differentiated, figure (20) shows the differentiated spectrum with Gaussian distribution for each signal, i.e. the step near the silicon surface, when differentiated, a negative Gaussian appeared. The full width half maximum FWHM of this Gaussian with the other signals divided by the location of each peak centroid, averaged, is conventionally the energy resolution of the backscattering system. (Knoll, 1979). The calculated resolution of the detector used in this work is 36 keV.

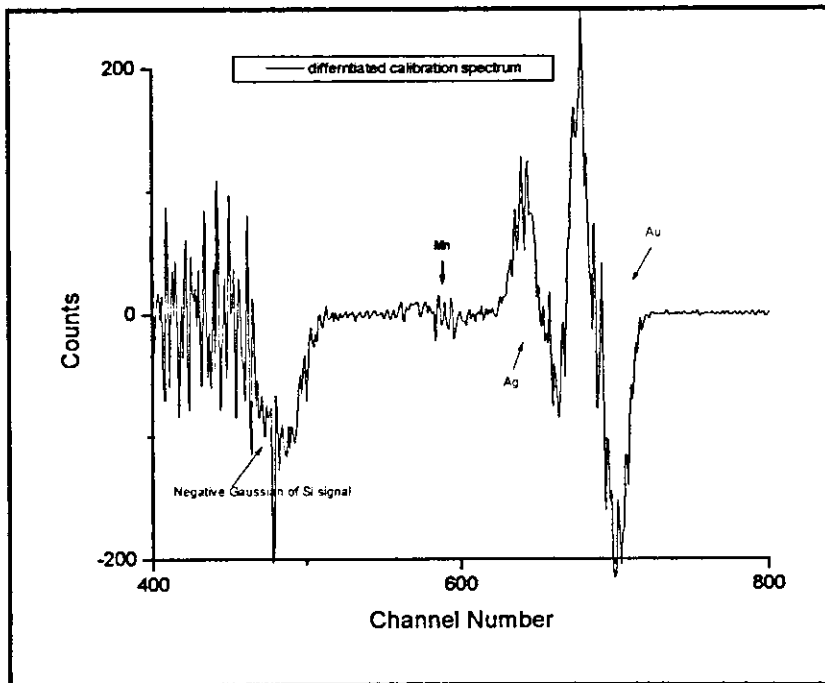


*Figure (20): Derivative RBS spectrum of the calibration sample.*

### 3.4 Sample Preparation

A number of extracted non-restored human teeth were collected from different dental clinics, including male and female teeth covering a wide range of ages, different types of tooth such as incisors, canines, molars and premolars, carious and sound teeth.

The tooth samples were brushed, washed in distilled water, dried, and cut off of their roots using a wafering diamond blade. After that, the prepared tooth samples were treated with two different commercially available fluoride containing dentifrices with various concentrations; Sodium Fluoride (NaF) and Sodium Mono-Fluoro-Phosphate (SMFP) so that the teeth enamel were topically fluoridated during 24 hours. Table (4) shows a brief description of tooth samples' preparations used in this work.

**Table (4): Brief description of subjected tooth samples.**

<i>Sample</i>	<i>Chemical state</i>	<i>Age</i>	<i>Type</i>	<i>Fluoride compound</i>	<i>Concentration of fluoride</i>
T <sub>1</sub>	Sound	17	Premolar	SMFP	1450ppm
				NaF	1350ppm
T <sub>2</sub>	Sound	40	Molar	SMFP	1450ppm
				NaF	1350ppm
T <sub>3</sub>	Caried	64	Incisor	SMFP	1450ppm
				NaF	1350ppm
T <sub>4</sub>	Sound	10	Canine	SMFP	1450ppm
				NaF	1350ppm

### **3.5 Experimental method**

#### ***3.5.1 Calibration using RBS***

A random tooth sample was bombarded with a beam of  ${}^4\text{He}$  ions of energy equals to 2 MeV for the purpose of calibration of the tooth enamel. The scattered  $\alpha$ -particles at an angle of  $135^\circ$  were detected by a surface barrier detector with an active area of  $150\text{ mm}^2$  and thickness of  $100\text{ }\mu\text{m}$ . The counts accumulated using a multichannel analyzer produced an  $\alpha$ -spectrum, which reveals several peaks related to the main elements composing the enamel of the subject tooth cf. figure (21)

Using equations (26) and (23), one becomes familiar with each element associated with a significant channel number in the  $\alpha$ -spectrum shown in figure (21). It is obvious that the tooth enamel generally consists of Oxygen, Sodium, Phosphor, and Calcium, see table (5). However, fluoride signal is apparently obscured, since RBS technique cannot detect low-mass elements in the presence of heavier ones. Data and relevant measurements are discussed in chapter four.

#### ***3.5.2 Depth Profiling using NRA***

The determination of the concentration profile of fluoride in tooth enamel is a favourable case for the nuclear resonance method (Mandler et al, 1973); the use of the  ${}^{19}\text{F}(p,\alpha){}^{16}\text{O}$  reaction has been shown to be a sensitive method for the detection of fluorine. This reaction exhibits many resonances which results in the emission of  $\alpha$ -particles with different energies, the resonance of prime concern for this work is the one at proton energy of 1350 keV. The proton energy varied from 1350 keV to 1400 keV in six steps, thus facilitating the profile measurements, that allows fluoride to be profiled to a depth of ( $1\text{ }\mu\text{m}$ ) in enamel.

However, in practice, the surface of the tooth enamel is not smooth and the influence of the surface roughness on the depth resolution must be considered, so the total depth resolution  $\Delta x_{total}$  is the result of the convolution of the surface roughness depth resolution and the ideal smooth target depth resolution. For enamel  $\Delta x_{total}$  varies between 500 to 800 nm in the first 1  $\mu\text{m}$  surface region of the material at an incident angle of  $0^\circ$ . (Plier et al, 1992).

It was mentioned before that in order to perform quantitative analysis for the determination of fluoride concentration in tooth enamel as a function of depth; a reference material is used as a standard. However, in this work,  $\text{CaF}_2$  was used as the standard sample of uniform fluoride concentration, in which the energy loss of either protons or  $\alpha$ -particles is approximately the same as in the tooth enamel that consists mainly of hydroxyapatite. Powder  $\text{CaF}_2$  was pressed in the form of a disc, then it was placed in the target chamber at the JUVAC and was bombarded with a beam of protons of incident energy equals to 1350 keV. Figure (23) shows the  $\alpha$ -spectrum produced after the nuclear reaction took place at the surface of the  $\text{CaF}_2$  sample.

Tooth samples were equilibrated with two different fluoride containing pastes; SMFP with a concentration of 1450ppm of fluoride, and NaF with a concentration of 1350 ppm of fluoride. Absolute fluoride concentrations in treated tooth samples were obtained by comparing measured yield of the  $\alpha$ -spectrum with data obtained from the control untreated tooth samples.

The measurements which provide the determination of the concentration profile and the fluorine uptake in tooth enamel were obtained by bombarding the samples with a proton beam of current less than 10 nA with a total collected charge of 8  $\mu\text{C}$ , since teeth are excellent insulators and charging is a serious problem.

The beam is collimated to a diameter of 1 mm and is normally incident, the nuclear reaction  $^{19}\text{F}(p,\alpha)^{16}\text{O}$  takes place at the surface of incident energy (1.350 MeV), yields high energetic  $\alpha$ -particles (7.1 MeV) which can be separated from the other  $\alpha$  groups that are produced when protons react with other isotopes than the only  $^{19}\text{F}$  stable isotope in tooth enamel.

**Table (5): Quantitative analysis for determining basic elements in teeth**

Channel Number associated with each peak	Kinematic factor (k) using: $KE_o (keV) = 3N - 219.2$	Rel. atomic Mass ( $M_2$ ) using: $K = \frac{E_1}{E_o} = \left[ \frac{M_1 \cos \theta + (M_1^2 - M_1^2 \sin^2 \theta)^{1/2}}{M_1 + M_1} \right]^2$	Element Associated with ( $M_2$ )
361	0.43	16	Oxygen
424	0.53	23	Sodium
510	0.65	31	Phosphorous
556	0.72	40	Calcium

It is well known that the basic compound forming human teeth is the hexagonal crystal hydroxyapatite,  $Ca_{10}(PO_4)_6(OH)_2$ . Theoretically, the ratio of the atomic densities of Oxygen  $N_O$  to that of Calcium  $N_{Ca}$  in this hydroxyapatite crystal is calculated as follows:

$$\frac{N_O}{N_{Ca}} = \frac{26}{10} = 2.6$$

On the other hand, measurements based on the RBS calibration, which was performed during the experiment; show that using the re-arranged form of equation (22), this ratio can be experimentally determined as follows:

$$\frac{C_O}{C_{Ca}} = \frac{H_O \sigma_{Ca}}{H_{Ca} \sigma_O} \quad (27)$$

where  $\frac{C_O}{C_{Ca}}$  is the ratio between the atomic densities of Oxygen to that of Calcium,

$H_O$  and  $H_{Ca}$  are the  $\alpha$ -yield of Oxygen and Calcium, respectively.  $\frac{\sigma_O}{\sigma_{Ca}}$  is the ratio of

the calculated Rutherford scattering cross section of Oxygen to that of Calcium at the incident helium ions energy of 2000 keV with a scattering angle of  $135^\circ$  using equation (25).



Consequently, performing these measurements and using the data shown in figure (21), one obtains the experimental ratio of the densities of Oxygen to that of Calcium:

$$\frac{C_o}{C_{Ca}} = \frac{135}{335} * \frac{0.6996}{0.1034} \cong 2.7$$

The obtained value is only about 4% higher than the expected one.

#### 4.2 Data Analysis

The resonant  $^{19}\text{F}(p,\alpha)^{16}\text{O}$  reaction at (1.35 MeV) proton energy yields high energetic  $\alpha$ -particles at (7.1 MeV) which is separated from other yield and any other  $\alpha$ -particle group resulting from protons reacting with nuclides presented in the matrix.

Quantitative analysis including determination of the relative concentrations of fluoride in tooth samples as a function of depth can be done using  $\text{CaF}_2$  as the standard sample since the energy loss of either protons (along the ingoing path) or  $\alpha$ -particles (through any outgoing longer path) is approximately the same as in tooth enamel. The values of energy loss suffered by protons per unit length  $dE/dx$  (or the stopping power values) at certain values of the incident proton energy are obtained using SRIM2003 computer program algorithm for both the standard target  $\text{CaF}_2$  and hydroxyapatite  $\text{Ca}_{10}(\text{PO}_4)_6(\text{OH})_2$ ; the basic mineral composing the tooth enamel. Those data are plotted in figure (22) and represent the stopping powers in units of (keV/microns) of the incident protons as a function of their energies for both targets.

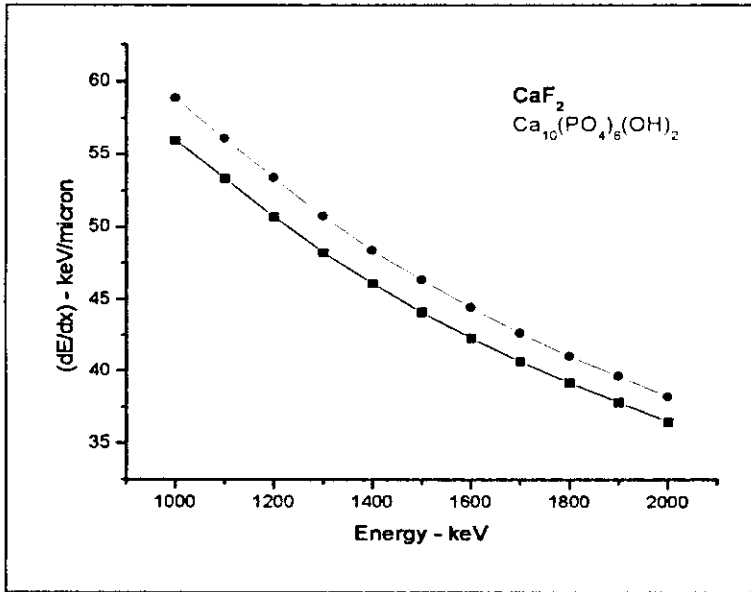


Figure (22): Stopping powers of protons in  $\text{CaF}_2$  and hydroxyapatite  $\text{Ca}_{10}(\text{PO}_4)_6(\text{OH})_2$

Figure (23) shows an  $\alpha$ -spectrum produced after the nuclear reaction  $^{19}\text{F}(\text{p},\alpha)^{16}\text{O}$  at 1.35 MeV takes place under the same experimental conditions of (10 nA) and total charge collected (8  $\mu\text{C}$ ) used in this experiment. The figure shows the energy spectrum of the produced  $\alpha$ -particles against channel number.

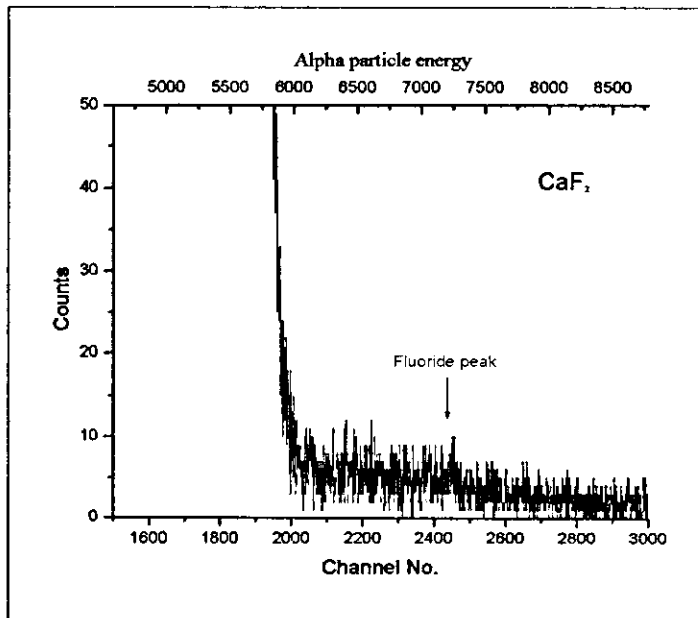


Figure (23):  $\alpha$ -spectrum emanating from  $\text{CaF}_2$

When a beam of protons of energy (1350) keV is incident on a light fluorine element within the target, the energy  $n(E_0)$  of the detected  $\alpha$ -particles resulting from the nuclear reaction  $^{19}\text{F}(p,\alpha)^{16}\text{O}$  is theoretically calculated; using equation (5) with the following values:

$$M_1 \equiv M_p = 1.008$$

$$M_2 \equiv M_i = 18.9984$$

$$M_3 \equiv M_O = 15.999$$

$$M_4 \equiv M_\alpha = 4.0026$$

$$Q = 8124 \text{ keV}$$

$$E_0 = 1350 \text{ keV, and } \theta = 135^\circ$$

Values of  $K_1$  and  $K_2$  are calculated, they are respectively, (2.609) keV and (7510.08) keV. These values are substituted in equation (5) to find  $n(E_0)$ ; the calculated energy of the detected  $\alpha$ -particles is approximately equal to (7100) keV.

On the other hand, the corresponding value of the average channel number of fluorine signal shown in figure (23) in the interval (2420-2440) is substituted in equation (26), to obtain the energy of the detected  $\alpha$ -particles experimentally, namely

$$E_{\alpha} = 3(2430) - 219.2$$

$$\cong 7100 \text{ keV}$$

Statistically, a fixed region of channel number is chosen through which the accumulated counts within the fluoride peaks are summed up in the standard sample as well as in all tooth samples for the purpose of determining the relative fluoride concentration versus depth profiles. The region in this work is chosen between the channel number 1370 and channel number 1470 that encloses the resonance region. The latter reveals the signal produced from fluoride in the target as shown in figure (23).

For correlating the energy spectra of  $\alpha$ -particles with depths in the targets one should study either the path of the incoming protons or the outgoing paths of the  $\alpha$ -particles emerging from the target.

Using the stopping powers values ( $dE/dx$ ) of the protons as function of the incident energies along the ingoing paths in both the standard sample  $\text{CaF}_2$  and the tooth samples  $\text{Ca}_{10}(\text{PO}_4)_6(\text{OH})_2$  obtained previously using SRIM2003 program one can depth profile. Table (6) illustrates the calculated values of slabs of thickness  $\Delta x$  traversed by protons in both the standard sample  $\text{CaF}_2$  and the tooth samples  $\text{Ca}_{10}(\text{PO}_4)_6(\text{OH})_2$  at each incident proton energy using equation (13).

**Table (6): values of the thickness traversed in both the standard  $\text{CaF}_2$  and the tooth samples  $\text{Ca}_{10}(\text{PO}_4)_6(\text{OH})_2$  at each incident proton energy.**

Incident proton energy (keV)	Energy loss in the target $\Delta E$ (keV) ( $E_{\text{Incident}} - E_{\text{Resonance}}$ )	$dE/dx$ (keV/ $\mu\text{m}$ )	$\Delta x$ ( $\mu\text{m}$ )	$dE/dx$ (keV/ $\mu\text{m}$ )	$\Delta x$ ( $\mu\text{m}$ )
		$\text{CaF}_2$	$\text{CaF}_2$	$\text{Ca}_{10}(\text{PO}_4)_6(\text{OH})_2$	$\text{Ca}_{10}(\text{PO}_4)_6(\text{OH})_2$
1350	0	47.157	0.00	49.579	0.00
1360	10	46.966	0.21	49.353	0.20
1370	20	46.744	0.43	49.003	0.41
1380	30	46.521	0.64	48.876	0.61
1390	40	46.298	0.86	48.653	0.82
1400	50	46.075	1.06	48.399	1.01

This table shows how proton energy loss increases as protons penetrate deeper in the target. Obviously a layer of (0.21) microns in  $\text{CaF}_2$  corresponds to a layer of (0.20) microns in tooth enamel. The standard sample  $\text{CaF}_2$  is profiled to a depth of (1.06)  $\mu\text{m}$  while tooth samples  $\text{Ca}_{10}(\text{PO}_4)_6(\text{OH})_2$  are profiled to a depth of (1.01)  $\mu\text{m}$ . Figure (24) shows depth traversed by both targets corresponding to each incident proton energy.

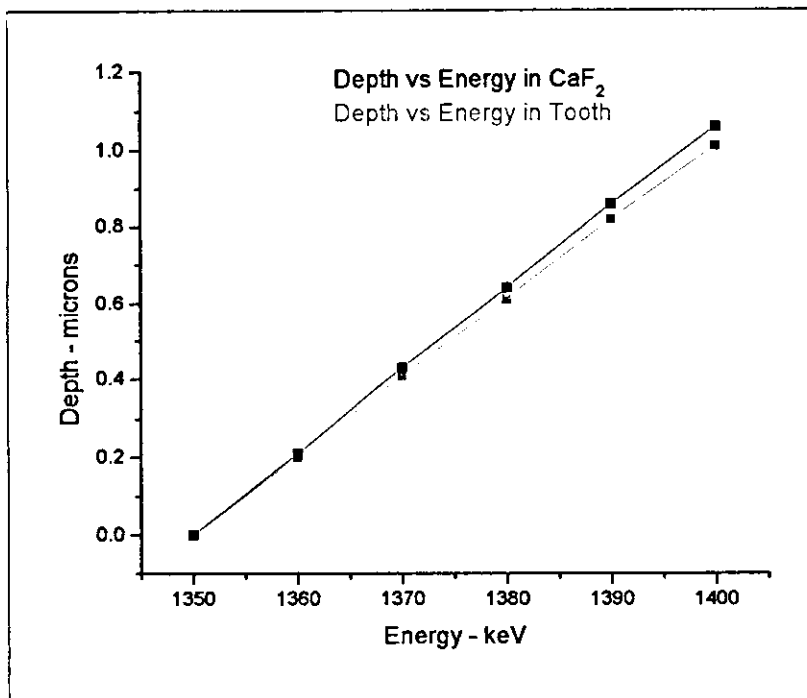


Figure (24): Depth values traversed at each incident proton energy.

## 4.3 Results and Discussion

### 4.3.1 Untreated Tooth Samples

Figures 25 through 28 show respectively the nuclear reaction spectra resulting from protons incident on the enamel of four untreated tooth samples, namely T<sub>1</sub>, T<sub>2</sub>, T<sub>3</sub>, and T<sub>4</sub> using the nuclear reaction  ${}^9\text{F}(p,\alpha){}^{16}\text{O}$  with incident proton energies varying between 1350 keV and 1400 keV in steps of 10 keV. Clearly the signal at low incident proton energies increases gradually as the incident energy increases until resonance, where it reveals the fluoride signal resulting from the nuclear reaction  ${}^9\text{F}(p,\alpha){}^{16}\text{O}$ , then the  $\alpha$ -signal decreases. The 7100 keV  $\alpha$ -particles detected at resonance and the neighbouring areas are integrated. The normalized integrated yield of the  $\alpha$ -signal at resonance; referred to as the relative fluoride concentrations, as a function of the incident proton energy is illustrated in figure (29).

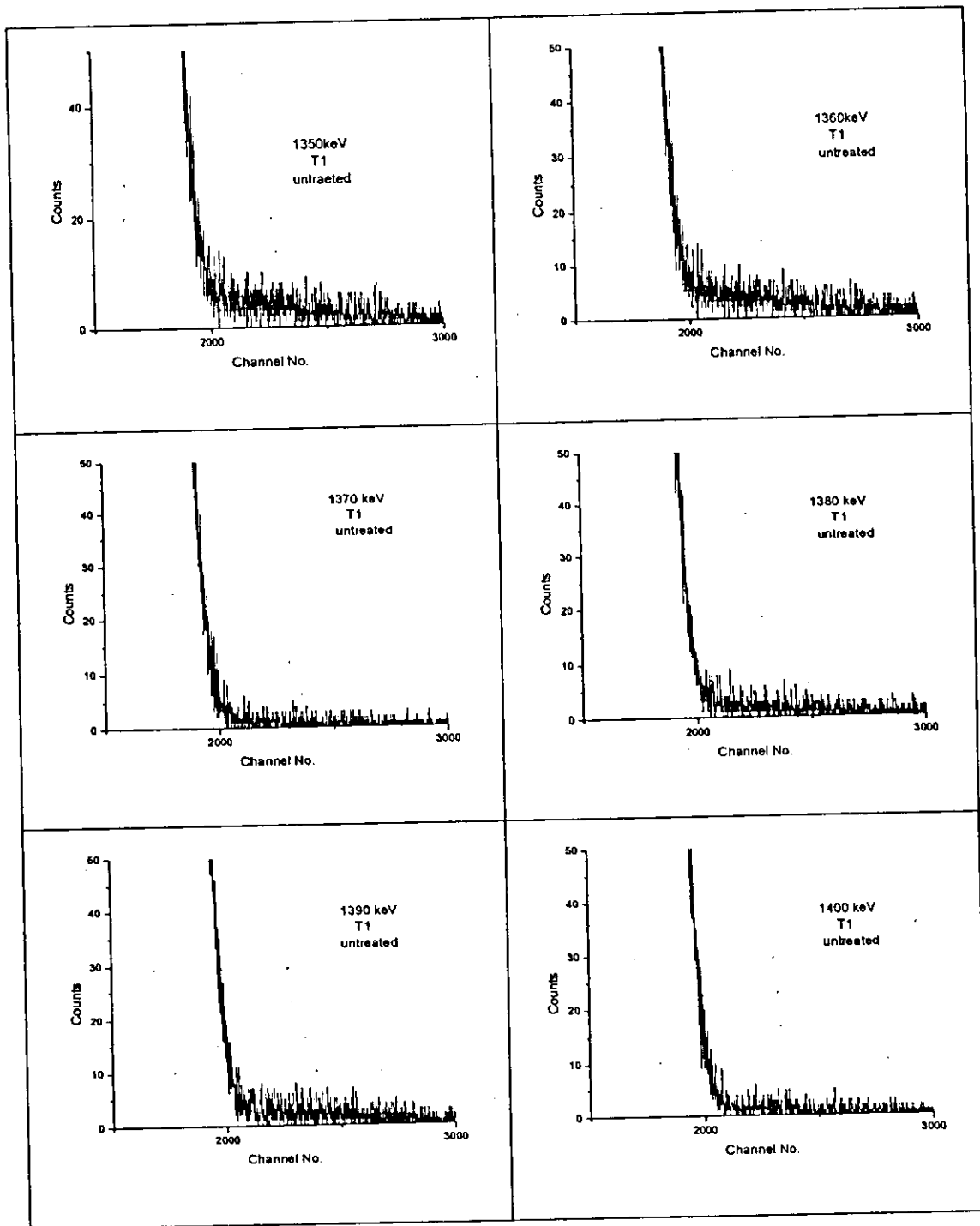


Figure (25):  $\alpha$ -spectra obtained after bombarding untreated tooth T<sub>1</sub> with a proton beam. The energy is indicated on each figure.

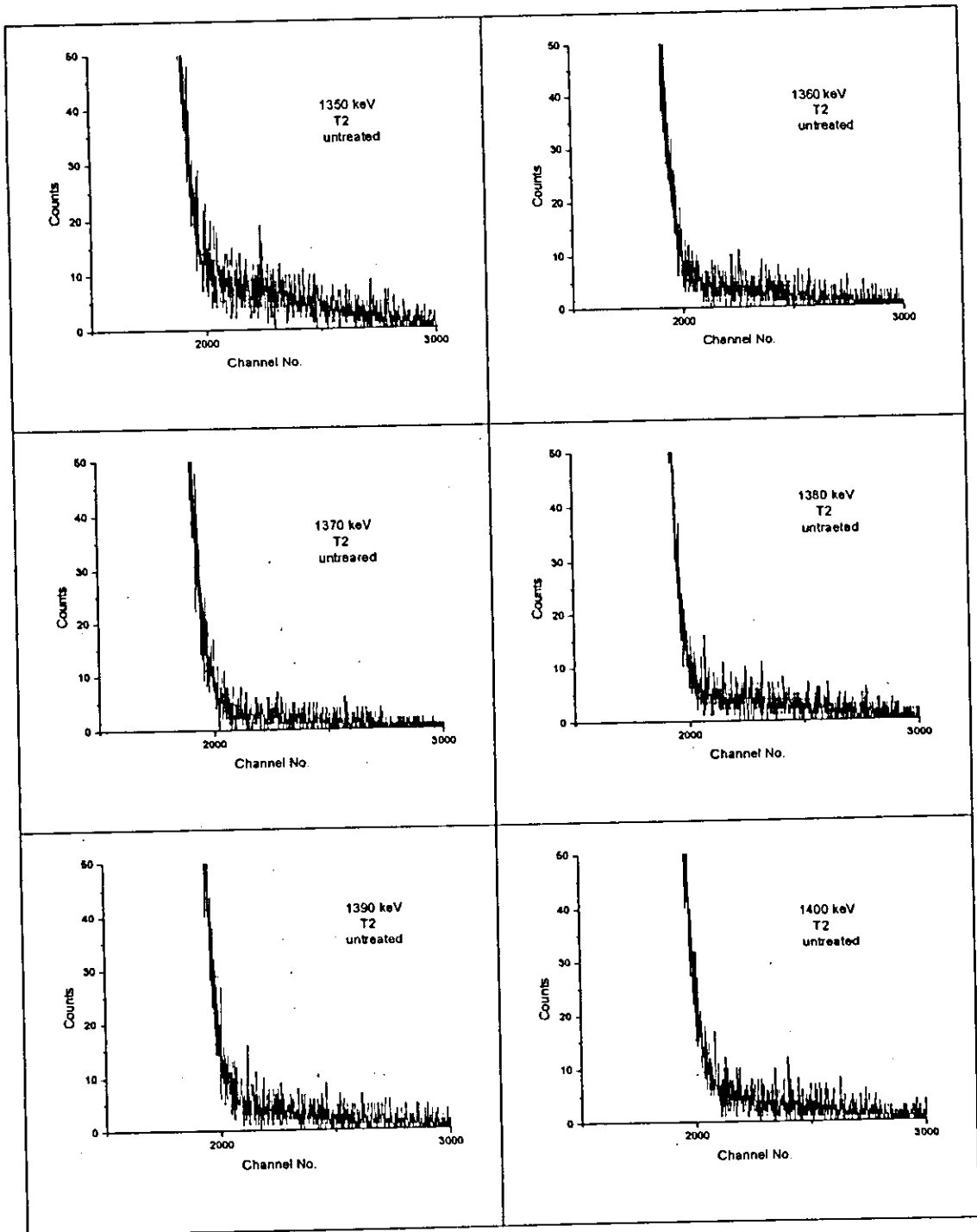


Figure (26):  $\alpha$ -spectra obtained after bombarding untreated tooth T<sub>2</sub> with a proton beam

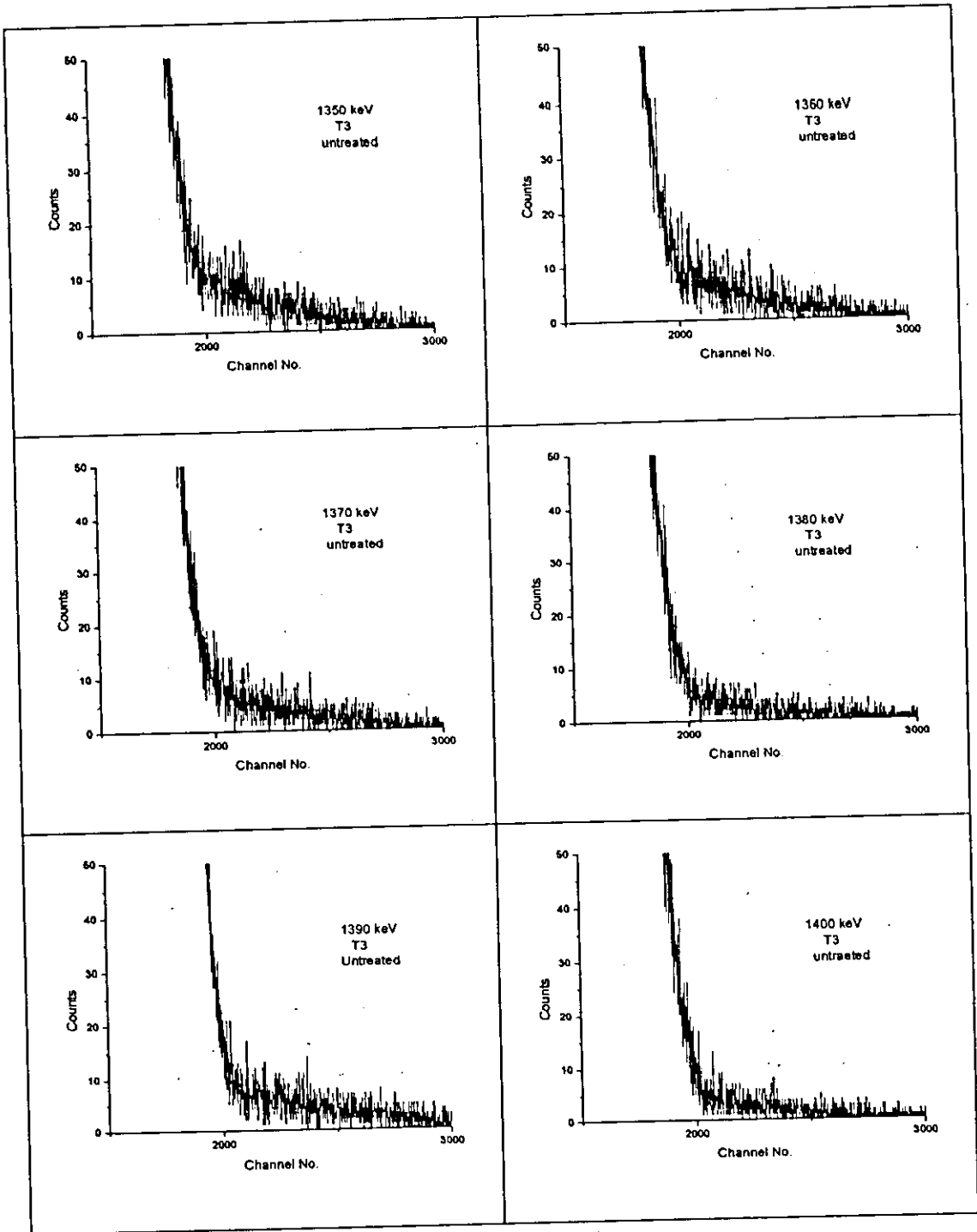


Figure (27):  $\alpha$ -spectra obtained after bombarding untreated tooth  $T_3$  with a proton beam



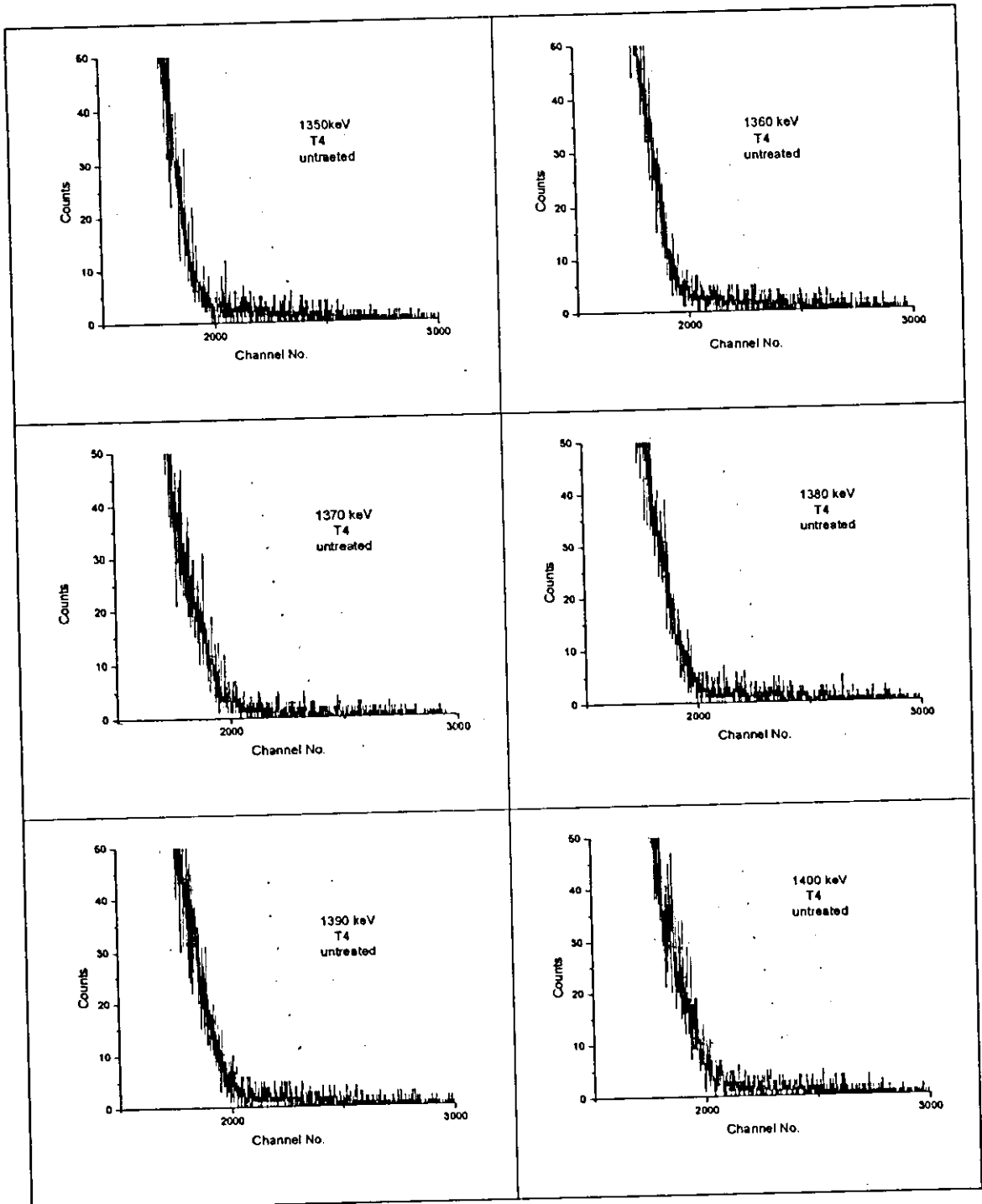
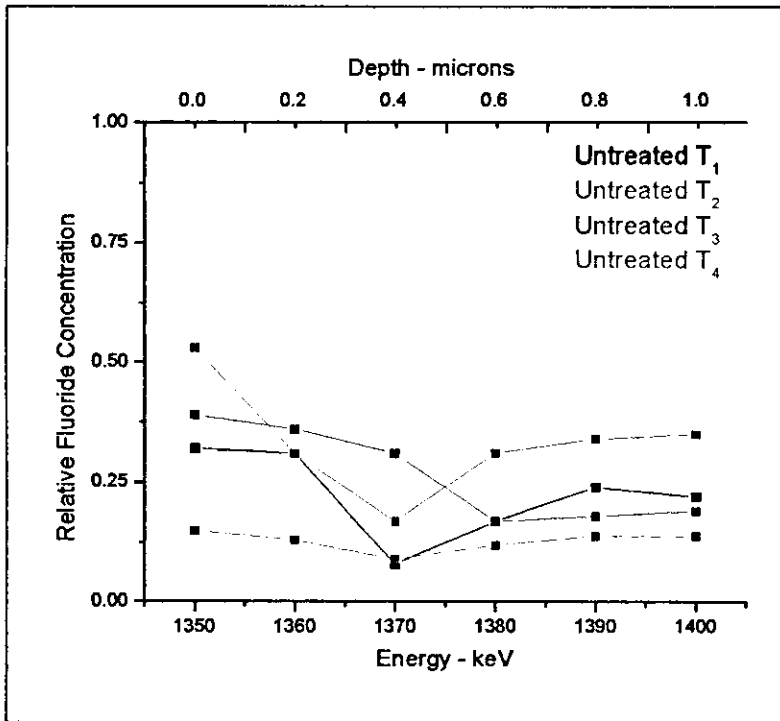


Figure (28):  $\alpha$ -spectra obtained after bombarding untreated tooth T<sub>4</sub> with a proton beam



*Figure (29): Relative Fluoride Concentrations in untreated tooth samples vs. Incident proton Energy.*

Figure (29) shows that the relative fluoride concentrations in T<sub>1</sub>, T<sub>2</sub>, and T<sub>4</sub> exhibit a tendency towards decreasing its value to a depth of (0.41) microns of the teeth surface value. The concentration then levels off and remains relatively constant. This behaviour indicates the accumulation process of “topical” fluoride provided by dentifrices on the surface of the tooth enamel and the fact that “systemic” fluoride ingested with drinking water gets absorbed in the bloodstream and becomes part of the inner layers of the dental enamel. In fact T<sub>1</sub>, T<sub>2</sub> samples represent the teeth of mid-aged humans with different fluoride concentrations that reflect the variations of the patient’s dietary habits and their backgrounds. On the other hand, T<sub>3</sub> exhibits fluoride concentration that decreases to a depth of (0.61) microns and afterwards an increase to a constant level is noted. This sample is however extracted from a 64-year old patient. Finally, T<sub>4</sub> which happens to be a sample tooth belonging to a 10-year old patient represents the lowest fluoride concentration among other samples.

### 4.3.2 Treated Tooth Samples

A sample of  $\alpha$ -spectra produced from bombarding a tooth sample, namely T<sub>1</sub> treated with NaF containing toothpaste with proton beam is presented in figure (30).

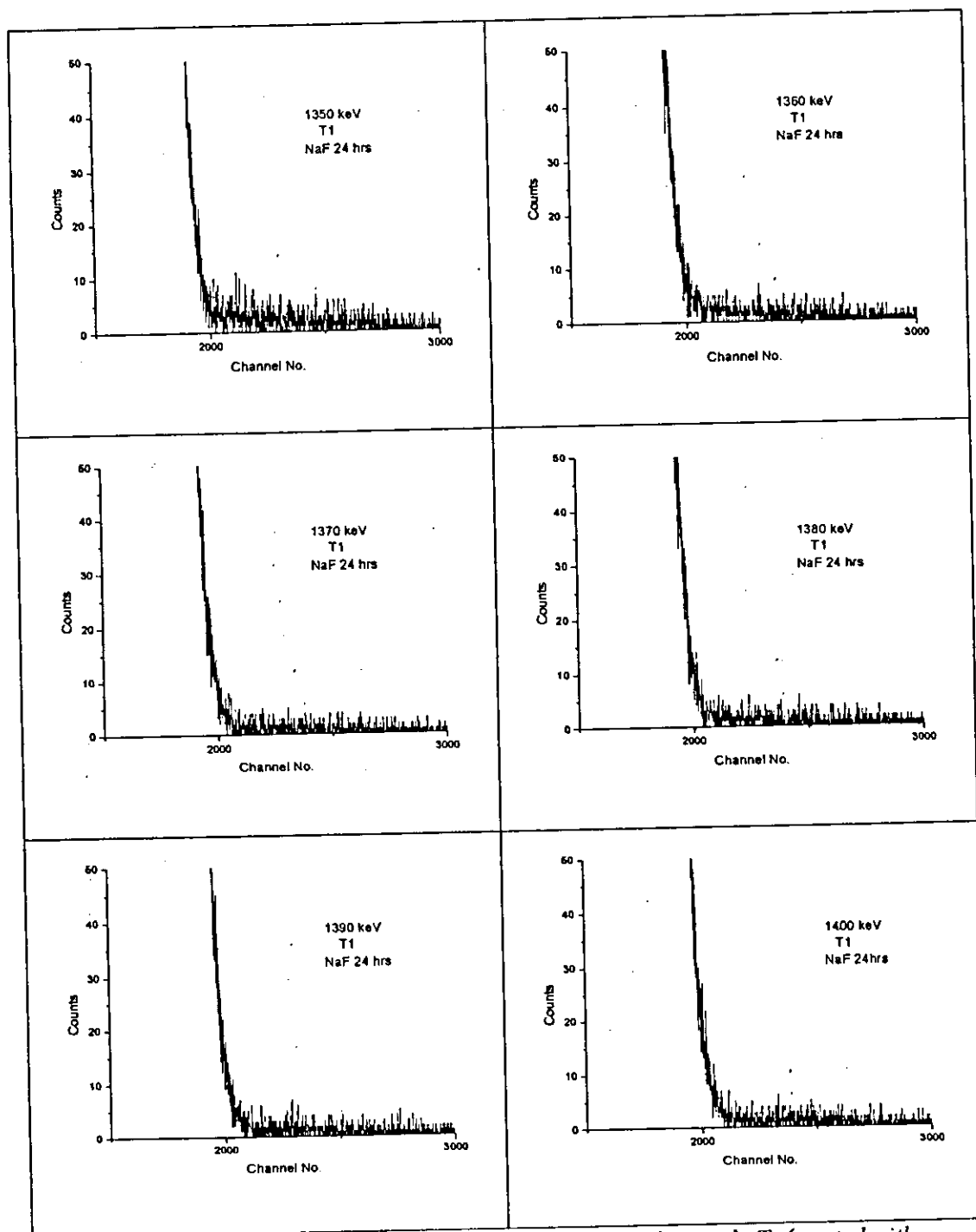


Figure (30):  $\alpha$ -spectra obtained after bombarding a tooth sample T<sub>1</sub> (treated with NaF containing dentifrice) with a proton beam.

Figure (31) shows the  $\alpha$ -spectra produced after bombarding the same tooth;  $T_1$  treated with Sodium Monofluoro-Phosphate (SMFP) containing toothpaste with various proton beam energies.

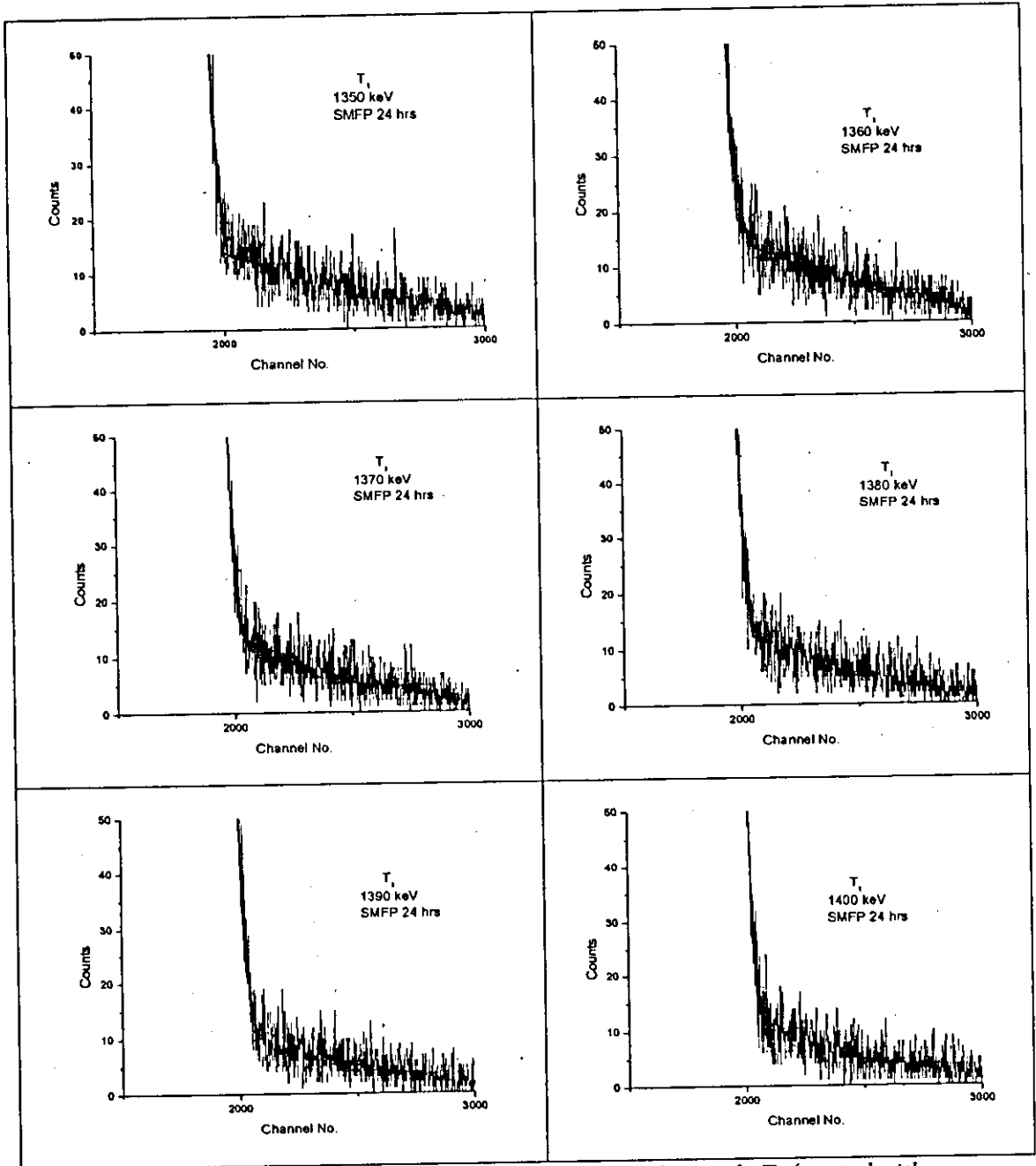


Figure (31):  $\alpha$ -spectra obtained from bombarding a tooth sample  $T_1$  (treated with SMFP containing dentifrice) with a proton beam.

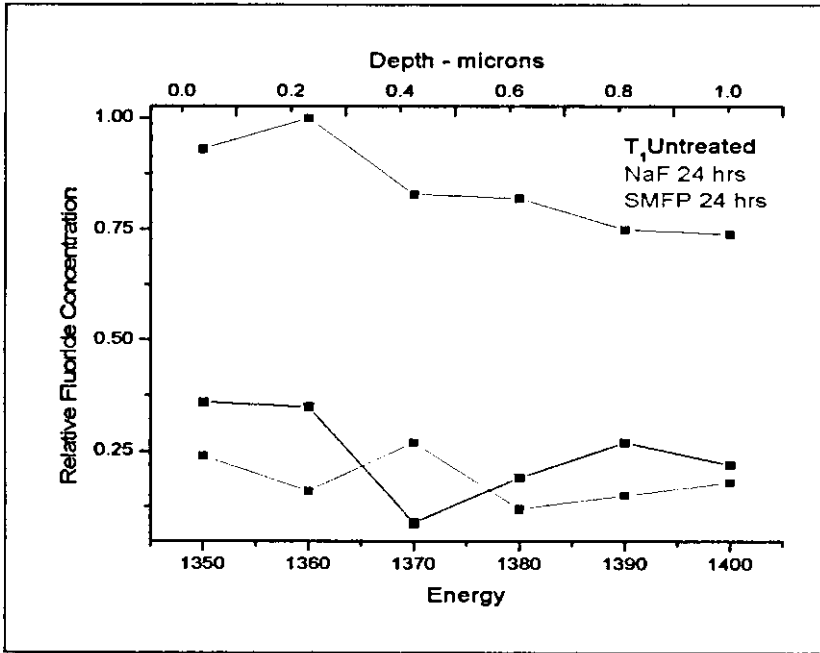


Figure (32): Relative Fluoride Concentrations in T<sub>1</sub> (Before treatment, after treatment with NaF, and after treatment with SMFP)

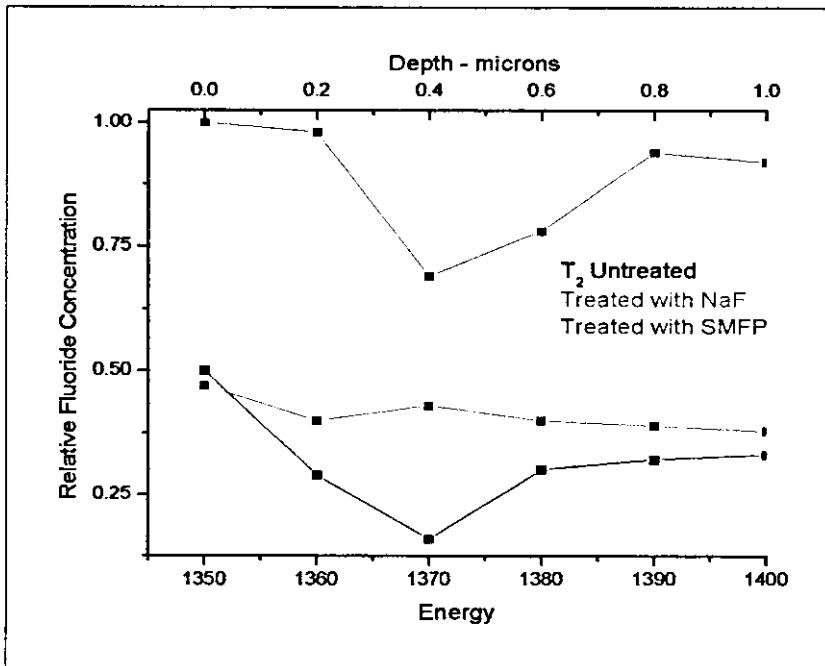


Figure (33): Relative Fluoride Concentrations in T<sub>2</sub> (Before treatment, after treatment with NaF, and after treatment with SMFP)

603373

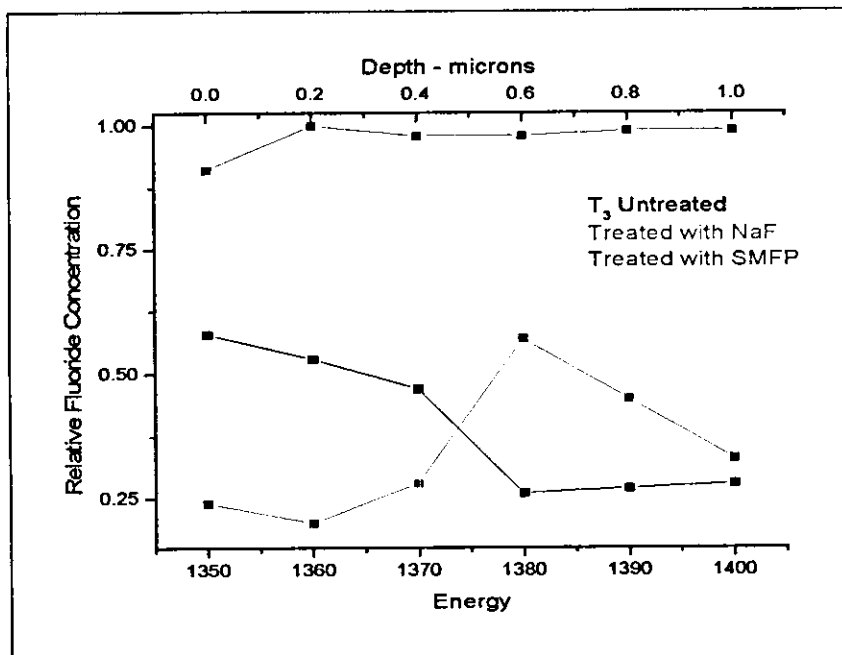


Figure (34): Relative Fluoride Concentrations in  $T_3$  (Before treatment, after treatment with NaF, and after treatment with SMFP)

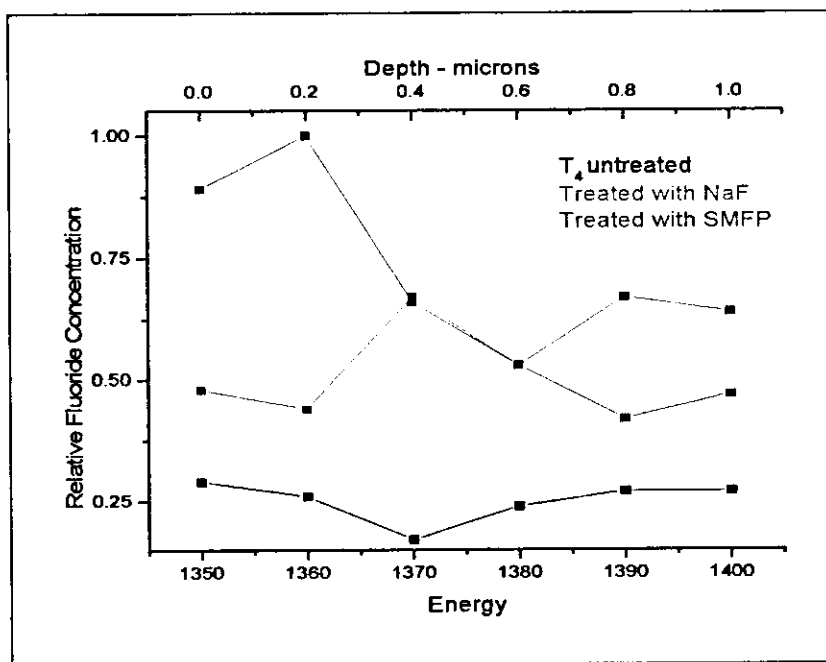
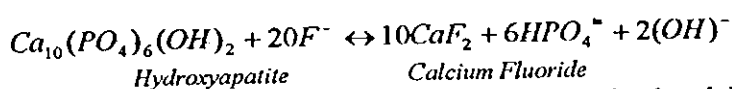


Figure (35): Relative Fluoride Concentrations in  $T_4$  (Before treatment, after treatment with NaF, and after treatment with SMFP)

Any consequent changes in the fluoride concentration in tooth samples after the application of NaF containing toothpaste with fluoride concentration (1350 ppm) to the untreated samples of the same teeth are shown in figures (32-35). The figures illustrate that immediately after NaF application a strong increase in the fluoride concentration occurred in sites of the enamel containing low fluoride pre-concentration.

On the other hand, the observed results illustrate a decrease in fluoride concentration near those sites of the dental enamel with relatively high fluoride pre-concentration, in particular, at the surface of the enamel. While it was initially postulated the effectiveness of topically applied NaF with fluoride concentration of (1350 ppm) was due to the formation of a fluor-hydroxyapatite, subsequent investigations indicated that the primary reaction product involved the transformation of surface hydroxyapatite to calcium fluoride according to:



The previous equation indicates that the reaction involves the breakdown of the apatite crystal into its components followed by the reaction of fluoride and calcium ions to form calcium fluoride with a net loss of phosphate ions from treated enamel. Newer fluoride systems however incorporate a means to prevent such phosphate loss. It has been suggested that the calcium fluoride formed on the enamel following a topical fluoride application has two possible fates: a portion of the initial reaction product undergoes further reaction, resulting in the formation of fluor-hydroxyapatite, while the remainder is lost from the enamel surface to the dental plaque or saliva. It is also recognized that the formation of fluor-hydroxyapatite in this manner is relatively slow and inefficient process.

Early investigations of the reaction between soluble fluoride and enamel indicated that the nature of the reaction products was markedly influenced by a number of factors, including fluoride concentration, the pH of the solution, and the length of exposure. For example the use of acidic fluoride solutions greatly favoured the formation of calcium fluoride. Neutral sodium fluoride solutions with fluoride concentrations of 100 ppm or less resulted primarily in the formation of fluoro-hydroxyapatite, while higher fluoride concentrations resulted in the formation of calcium fluoride (Christen 1991). Another example is presented by (Chedid and Cury, 2004) shows the lack of effect of 0.02% NaF solution compared to other fluoridated dentifrices.

Moreover, the previous figures show the remarkable high dental uptake of fluoride by the same tooth samples treated with Sodium Mono-Fluoro Phosphate ( $\text{Na}_2\text{PO}_3\text{F}$ ) containing gel. SMFP has been evaluated and approved for use in dentifrices as an agent for fluoride topical application. Although the mechanism of action of SMFP is thought to involve a chemical reaction with surface enamel, the precise nature of this reaction is poorly understood. Some have suggested that the fluorophosphates moiety,  $\text{PO}_3\text{F}^-$  dissociates into  $\text{PO}_3^-$  and  $\text{F}^-$  with the ionic fluoride reacting with hydroxyapatite. During the 1960s a number of reports of clinical trials indicated that the use of SMFP in dentifrices contributed significantly to the control of dental caries for its interesting characteristic of being compatible with a wide variety of dentifrice abrasive systems in contrast to other fluoride compounds such as NaF.

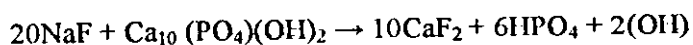


It appears that the predominant mechanism of action of fluoride is its ability to facilitate the remineralisation of the demineralised areas. Topically applied fluoride clearly diffuses into these demineralised areas and reacts with calcium and phosphate to form fluorhydroxyapatite in the remineralisation process. As a result, topical fluoride applications appear to be an effective means of inducing the remineralisation of incipient lesions.

## CHAPTER FIVE

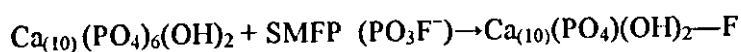
### 5.1 CONCLUSIONS

1. The main conclusion to be drawn from this study is that nuclear techniques can successfully be applied to give information concerning the fluoride profile in tooth enamel where differences in the magnitude of the fluoride concentrations and fluorine concentration as a function of depth are easily detected.
2. Fluoride concentration in teeth varies depending on the age and dietary habits of the patient.
3. The fluoride uptake decreased as the fluorine pre-concentration in the enamel increased.
4. Fluoride was preferentially taken up in demineralized (caried) enamel, these results show that fluoride uptake, after the NaF varnish is applied, is directly connected with the mineralization processes at the enamel surface.
5. Application of SMFP can be better than that of NaF of certain concentrations, reason:



There is a loss of P and the  $\text{CaF}_2$  is formed is smaller than hydroxyapatite.

But:



Fluorhydroxyapatite is formed; which is a bigger molecule than hydroxyapatite (P is not lost).

## 5.2 FUTURE WORK

- 1- A short demineralization of enamel, before an application of fluoride containing varnish is suggested that can lead to a long term deposition of fluoride in enamel, i.e. acidic medium can be applied to part of the samples directly before the application of NaF containing varnish to increase fluoride uptake.
- 2- Time of topical fluoride exposure can be varied using the same fluoride containing gel with a constant concentration to verify the effect of the factor of time.

## References

- J. P. Thomas and A. Cachard, **Material characterization using Ion Beams**, Plenum Press, 1978.
- Wei-Kan Chu, James W. Mayer, and Marc-A Nicolet, **Backscattering Spectrometry**, Academic Press INC. 1978.
- W. M. Gibson, **Nuclear Reactions**, Penguin Books Ltd. Harmondsworth, Middlesex, England 1971.
- G. Götz and K. Gärtner, **High Energy Ion Beam Analysis of Solids**, 1986.
- P. Mazzoldi and George W. Arnold, **Ion Beam Modification of Insulators, Beam Modification of Matter 2**, Elsevier, 1987.
- H. H. Anderson and J. F. Ziegler, **Hydrogen, Stopping Powers and Ranges in all Elements**, Volume 3, Pergamon, 1977.
- J. W. Mayer and E. Rimini, **Ion Beam Handbook for Material Analysis**, Academic Press, 1977.
- F. Glenn Knoll, **Radiation Detection and Measurements**, John Wiley & Sons, 1979.
- M. Baumann Scott, 2000, <http://www.cca.com/cai/rbstheo/intro/html>.
- Christen **Preventive Dentistry**, 3<sup>rd</sup> Edition, Norwalk, Appletton and Lange, 1991.
- Martha Keene, and Anne Griffin Perry, **Second Edition**, 2002.
- M-A. Mayer, Nicolet, and J.W. Mitchell. I.V. **Thin Solid Films**, 17 1 (1973).
- G. E. Coote, **Nucl. Inst. and Meth.** B66 (1-2) (1992) 191-204.
- R. F. Sippel and E. D. Glover, **Nucl. Inst. and Meth.** 9 (1960) 37.
- J. W. Mandler, R. B. Moler, E. Raisen and K. S. Rajan, **Thin Solid Films**, 19 (1973) 165.
- L. Torrisi, K. Sheng, E. Rapisarda and G. Foti, **Il Nuovo Cimento**, Vol. 5D No. 2, (1986) 164.
- J.D. Borgardt, M. D. Ashbaugh, L. C. Mclztyre Jr., J. O. Stoner Jr., R. B. Gegory, M. Azrak, and J. Wetzel, **Nuclear Instruments and Methods in Physics Research**, B136-138 (1998) 528-532.
- M. L. Carvalho, A. G. Karydas, C. Casaca, Ch. Zarkadas, **Nuclear Instruments and Methods in Physics Research**, B179 (2001) 561-567.

- F. Plier, H. E. Zschau and G. Otto, **Nuclear Instruments and Methods in Physics Research**, B66 (1992) 295-297.
- G. Amsel, J. P. Nadai, E. D'arternare, D. David, E. Girard and J. Moulin, **Nucl. Inst. and Meth.** 92 (1971) 481-498.
- D.-E. Arafah and J. D. Meyer, **J. Applied Physics** 64 (3) (1988) 1557.
- G. N. Jenkins, **Int. Dent. J.** 17 (1967) 552.
- M. E. J. Cueson and F. L. Losee, **JADA** 94 (1977) 1146.
- J. Kuperus, **Physica**, 31 (1965) 1603.
- M. A. Chaudhri and A. Crawford, **Nuclear Instruments and Methods in Physics Research**, B181 (1981) 327.
- H. J. Annegarn, A. Jodaikin, P. E. Cleaton-Jones, J. P. F. Sellschop, C. C. P. Madiba, and D. Bibby, **Nuclear Instruments and Methods in Physics Research**, B181 (1981) 323.
- Rosin-Grget and Lincir 2001, Mellberg 1997, and Rolla 1993.
- A. Savidou, X. Aslanoglou, T. Parradellis. And M. Pilakouta, **Nuclear Instruments and Methods in Physics Research**, B152 (1999) 12-18.
- K. Ishi, M. Valladon, C. S. Sastri, and J. L. Deburn, **Nucl. Inst. and Meth.** 153 (1978) 503.
- G. Amsel and W. A. Lanford, **Rev. Nucl. Part. Sci**, 34 (1984) 435.
- M. Navarro, L. A. Monte Alto, R. A. Cruz, and J. Prazeres, **Braz. Dent. J**, 12(3) (2001) 178-182.
- S.J. Chedid , Cury JA. Effect of 0.02% NaF solution on enamel demineralization and fluoride uptake by deciduous teeth in vitro. **Braz Oral Res** 2004; **18 (1): 18-22.**
- K.W. Stephen ,Chestnutt IG, Jacobson AP, McAll DR, Chesters RK, Huntigton E, Schafer F. The effect of NaF and SMFP toothpastes on three-year caries increments in adolescents. **Dept of Adult Dental Care, UK.**
- M. Leon Silverstone **Preventive Dentistry**, London Fort Lee, 1978.
- R. Z. Le Geros, **Calcium phosphates in oral biology and medicine**, M. Howard Mayer, Ed., San Fransisco, California 1991.

دراسة لترسبات الفلور في المينا السنية بعد استخدام هلامي يحتوي الفلور

بواسطة التفاعل النووي  $(p, \alpha\gamma)$

إعداد

أناهيثا سهيل نصر

إشراف

أ.د. ضياء الدين عرفة

ملخص

قام أطباء الأسنان وفيزيائيون بتحليل امتصاص الفلور بأساليب فيزيائية نووية بعد أن عالجوا مينا السن المنخور بالعامل الوقائي. وتهدف هذه الدراسة الى معرفة مقدار الفلور المتبقي في عينات أسنان لعدة أشخاص مختلفين بعد أن تم معالجتها بمعجون تنظيف الأسنان يحتوي على مركب SMFP واخر يحتوي على مركب NaF.

إن استخدام تفاعل  $^{19}\text{F}(p, \alpha\gamma)^{16}\text{O}$  كاسلوب تحليلي في منطقة الرنين بإطلاق شعاع من البروتونات بطاقة (1350keV) من خلال مسارع فان دي غراف الموجود في الجامعة الاردنية (JUVAC) وتسجيل جسيمات  $(\alpha)$  المنبعثة بطاقة (7071 keV) تم تحديد تركيز الفلور من خلال مقارنة مقدار  $(\alpha)$  المنبعثة من عينة مرجعية من  $\text{CaF}_2$  وتوضح أن تركيز الفلور في مينا السن يعتمد على عمر وسلوك الحمية الغذائية عند المريض. وعلى أية حال فإن سلوك الفلور في عينات السن في عمق (1 $\mu\text{m}$ ) يشير إلى أن تركيز الفلور في عينة معينة تتناقص إلى عمق معين ثم تزداد.

إن امتصاص الفلور من العينات المعالجة بمعجون أسنان يحتوي على NaF يعتمد على مدى تركيز الفلور في هذه الأسنان قبل المعالجة في حين أن امتصاص الفلور من العينات المعالجة بمعجون أسنان يحوي SMFP كانت أكبر بكثير.